


# Experimental evidence of transverse modulation and frequency downshift of uniform waves in a long tank

Karsten Trulsen<sup>1</sup> , Carl Trygve Stansberg<sup>2,3</sup> and Kristian Barstad Dysthe<sup>4,†</sup>

<sup>1</sup>Department of Mathematics, University of Oslo, Oslo, Norway

<sup>2</sup>MARINTEK, Trondheim, Norway (now renamed SINTEF Ocean) until 2016

<sup>3</sup>CTStansberg Marinteknikk, Trondheim, Norway

<sup>4</sup>Department of Mathematics, University of Bergen, Bergen, Norway

**Corresponding author:** Karsten Trulsen, [karstent@math.uio.no](mailto:karstent@math.uio.no)

(Received 9 July 2025; revised 30 September 2025; accepted 6 October 2025)

We report experiments in a long tank showing that transverse Benjamin–Feir instability of Stokes waves can lead to a significant energy transfer into oscillations across the tank. We observe frequency downshift in the long-term evolution of Stokes waves essentially when significant energy is transferred to narrow-banded transverse modes. Experiments with Stokes waves are often carried out with wavelengths that are not long compared with the width of the tank, permitting transverse instabilities to be excited. With insufficient resolution of measurements across the tank, transfer of energy to transverse modes can be misinterpreted as dissipation. Our experiments suggest that the frequency downshift depends as much on energy-preserving transverse modulations of type I as it does on damping or wave breaking. Broad-banded unstable modulations of type II do not imply downshift.

**Key words:** surface gravity waves

## 1. Introduction

Uniform long-crested water surface waves of permanent form on deep water, commonly known as Stokes waves (Stokes 1847), are unstable to sideband perturbations. The instability was first discovered for narrow-band collinear perturbations (Lighthill 1965; Benjamin 1967; Benjamin & Feir 1967) and is commonly known as the Benjamin–Feir instability.

<sup>†</sup>Deceased July 30th, 2023

© The Author(s), 2025. Published by Cambridge University Press. This is an Open Access article, distributed under the terms of the Creative Commons Attribution licence (<https://creativecommons.org/licenses/by/4.0/>), which permits unrestricted re-use, distribution and reproduction, provided the original article is properly cited.

The collinear narrow-band instability vanishes for finite depth  $kh < 1.363$  (Benjamin 1967; Hasimoto & Ono 1972). Here,  $k = 2\pi/\lambda$  is the wavenumber,  $\lambda$  is the wavelength and  $h$  is the depth. The instability also extends to transverse perturbations which are unstable for both greater and smaller depths (Benney & Roskes 1969).

In the course of long-term evolution, following the initial instability, and after a stage of heavy modulations, there may be recurrence back to a uniform wave train. There is laboratory evidence that the recurrence can either be back to the original Stokes wave frequency or it can be accompanied by a downshift to a lower frequency (Lake *et al.* 1977). The downshift has been observed together with wave breaking and with the growth of a continuous background spectrum (Melville 1982; Tulin & Waseda 1999).

Simple model equations predict that the Fermi–Pasta–Ulam–Tsingou recurrence, in which the initial uniform wave train recurs (Fermi, Pasta & Ulam 1955; Dauxois 2008), also can happen for water waves (Yuen & Ferguson 1978*b*; Janssen 1981). Although a temporal downshift is predicted by the non-dissipative Dysthe equation for long-crested waves (Dysthe 1979; Janssen 1983; Lo & Mei 1985), a permanent recurrence with downshift was previously thought to depend on dissipative effects. A permanent downshift has been captured by long-crested model equations equipped with various types of dissipation, including *ad hoc* models for wave breaking (Trulsen & Dysthe 1990), models for viscous damping without breaking (Uchiyama & Kawahara 1994; Kato & Oikawa 1995; Skandrani, Kharif & Poitevin 1996; Segur *et al.* 2005; Islas & Schober 2011*a,b*), combinations of wind forcing and damping (Hara & Mei 1991; Trulsen & Dysthe 1992; Schober & Strawn 2015) and models for energy and momentum loss due to breaking (Tulin 1996; Tulin & Waseda 1999). A review of long-crested downshift with various dissipation mechanisms was given by Carter, Henderson & Butterfield (2019). Recently, Ratliff, Trichtchenko & Bridges (2025) suggested that the permanent downshift in the recurrence cycle of long-crested Stokes waves can be achieved without dissipation.

On the other hand, downshifting has also been observed in the undamped evolution of a finite-width spectrum (Onorato *et al.* 2002; Dysthe *et al.* 2003; Onorato *et al.* 2009; Chalikov 2012), however, we consider that to be an essentially different phenomenon partly due to the lack of recurrence to a uniform wave and partly due to the fact that a finite-width spectrum does not support the initial modulational instability (Alber 1978).

Stokes waves are unstable to infinitesimal perturbations due to both four-wave and five-wave nonlinear resonance. In McLean *et al.* (1981) these are denoted instabilities of types I and II, respectively. The Benjamin–Feir instability is of narrow-band type I. These instabilities are nicely summarised in figure 1 of McLean *et al.* (1981) from which it is observed that type I is nearly collinear and mostly narrow band while type II is mainly transverse and only wide band. Type I transverse instability of Stokes waves has been reported in experiments (Toffoli *et al.* 2013; Pinho & Babanin 2015). Type II instability of Stokes waves gives rise to characteristic horseshoe patterns of transverse length equal to the longitudinal wavelength (Su 1982; Su *et al.* 1982). Transverse modulations of narrow-band type I and broad-band type II are easily distinguished by visual inspection of the wave field, as can be appreciated in photos from our experiments in figure 1. Pictures from all the experiments are shown in Appendix B.

The emphasis of this paper is on the weakly nonlinear and narrow-banded transverse instability of type I. For sufficiently narrow wave tanks there is numerical evidence that non-dissipative transverse modulations can lead to recurrence without downshift (Yuen & Ferguson 1978*a*; Lo & Mei 1987). For slightly wider wave tanks there is numerical evidence of a permanent non-dissipative downshift to transverse modes (Trulsen & Dysthe 1997). Trulsen, Stansberg & Velarde (1999) provided experimental evidence that the downshift can be accompanied by substantial transfer of energy from long-crested modes



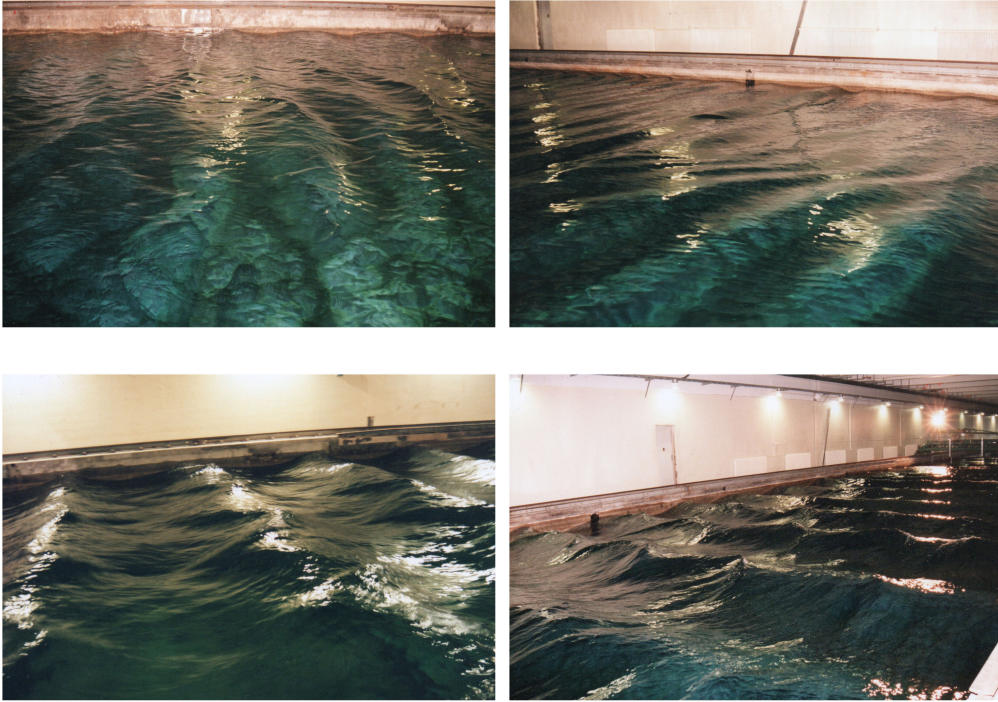


Figure 1. Upper left: Transverse modulation (TM) of type I in run 8008. Upper right: TM of type I in run 8015. Lower left and right: Horseshoe patterns typical of TM of type II in run 8012.

to transverse modes, which can easily be misinterpreted as dissipation in the case of insufficient measurements in the transverse direction. Accurate numerical simulations of short-crested waves by Fuhrman, Madsen & Bingham (2006) further support the conclusions of Trulsen & Dysthe (1997).

Trulsen & Dysthe (1997) and Trulsen *et al.* (1999) anticipated that the evolution with transverse modes depends on a width parameter  $\mu = k_{\perp}/k_c$ , where  $k_{\perp}$  is a permissible transverse wavenumber vector component, while  $k_c = 2\pi/\lambda$  is the characteristic wavenumber and  $\lambda$  is the characteristic wavelength of the original Stokes wave. In a wave tank of width  $b$  the permissible transverse wavenumber components will be discretised in multiples of  $\Delta k_{\perp} = \pi/b$  and the width parameter will be discretised in multiples of  $\Delta\mu = \Delta k_{\perp}/k_c = \lambda/(2b)$ . On deep water this evaluates to

$$\Delta\mu = \frac{\Delta k_{\perp}}{k_c} = \frac{\lambda}{2b} = \frac{gT^2}{4\pi b}, \quad (1.1)$$

where  $T$  is the characteristic wave period and  $g$  is the acceleration due to gravity. Transverse type I instability can be excited in experiments when  $\Delta\mu$  is small enough to be inside the unstable domain. In the figures of McLean *et al.* (1981) their  $q$  along the second axis is identical to our  $\mu$ , and our  $\Delta\mu$  is the discretisation along that axis. Visual inspection of figure 1 in McLean *et al.* (1981) suggests that the transverse instability of type I is contained within  $\mu < 0.36$ . From the same figure we also see that unstable perturbations of type II are essentially limited to  $\mu > 1$  for the small steepnesses  $\epsilon = a_c k_c < 0.33$  employed in our experiments. Here, we define the characteristic amplitude to be  $a_c = \sqrt{2}\sigma$ , where  $\sigma$  is the standard deviation of the surface elevation, thus for uniform waves  $a_c$  is the amplitude and  $H = 2a_c$  is the wave height.

The single experiment reported by Trulsen *et al.* (1999) had  $\Delta\mu = 0.074$ , with unseeded Stokes waves generated by the wave maker, and with transverse measurements limited to only one propagation distance along the tank, where only two probes were located across the tank. The original experiments of Lake *et al.* (1977) had  $\mu = 0.066$  (see Trulsen & Dysthe 1997) with only one probe across the tank. Toffoli *et al.* (2013) reported experiments with  $\Delta\mu$  between 0.011 and 0.031, with seeded Stokes waves with transverse modulations generated by the wave maker, unfortunately without transverse measurements. Pinho & Babanin (2015) reported experiments with  $\Delta\mu$  between 0.0094 and 0.026, with unseeded Stokes waves generated by the wave maker, and with transverse measurements limited to only one propagation distance along the tank where nine probes were located across the tank. Numerical simulations with  $\mu = 0.098$  and with seeded perturbations of Stokes waves reported by Fernandez *et al.* (2014) showed substantial growth of oblique sidebands.

There is a lack of experiments resolving the evolution of several transverse modes of Stokes waves propagating along a tank of finite width. We here report such experiments, with  $\Delta\mu$  between 0.05 and 0.15, with unseeded Stokes waves generated by the wave maker, and with transverse measurements using five probes across the tank at four distances along the tank. This gives adequate resolution for the unstable mode dynamics within the domain of the type I instability, while it does not resolve the dynamics of the type II instability. The presence of both type I and II modulations were, however, observed visually. These tests were run in a 260 m long and 10.5 m wide tank, which is long enough to study the problem at a reasonable scale.

This paper deals with the evolution of uniform waves in a long tank for the limiting regime that the tank is just wide enough for unstable transverse modulations to modify the long range evolution compared with a narrow tank. We discover that the limiting width corresponds to  $\Delta\mu \approx 0.1$ , thus the tank should accommodate crest lengths of at least 10 wavelengths. In this paper we do not consider the opposite limit of wide basins with  $\Delta\mu \ll 0.1$ , or irregular waves for which the modulational instability is suppressed (Alber 1978) such as Onorato *et al.* (2009), Toffoli *et al.* (2010) and Cherneva & Guedes Soares (2011) who employed irregular waves with small  $\Delta\mu = 0.016$ .

It is a curious coincidence, not necessarily related, that Gramstad & Trulsen (2007) concluded the Benjamin–Feir index is a good indicator of increased freak wave activity only when the wave field is long crested with characteristic crest length at least 10 characteristic wavelengths.

## 2. Experimental set-up

The experiments were carried out during the summer of 1998 in the towing tank at MARINTEK (later renamed SINTEF Ocean). The tank is 260 m long and  $b = 10.5$  m wide. The depth of the tank is  $h = 10$  m for the first 80 m closest to the wave maker, and  $h = 5$  m elsewhere, with a step-type bathymetric connection. The experimental set-up, using 20 probes arranged with five across the tank at four distances from the wave maker, is shown in figure 2. The  $x$ -axis runs along the tank measuring the distance from the wave maker. The  $y$ -axis is across with  $y = 0$  at one side. The probes are at transverse positions  $y_l = lb/6$  for  $l = 1, 2, 3, 4, 5$ , between the lateral tank walls at  $y = 0$  and  $y = b$ . The wave tank is sufficiently long that waves reflected from the damping beach do not reach back within the time window used for analysis.

The experiments consisted of generating long series of un-seeded uniform long-crested waves, with crests aligned in the  $y$ -direction, with given period  $T$  and wave height  $H$ . Unstable perturbations grew naturally and the resulting modulations were recorded by

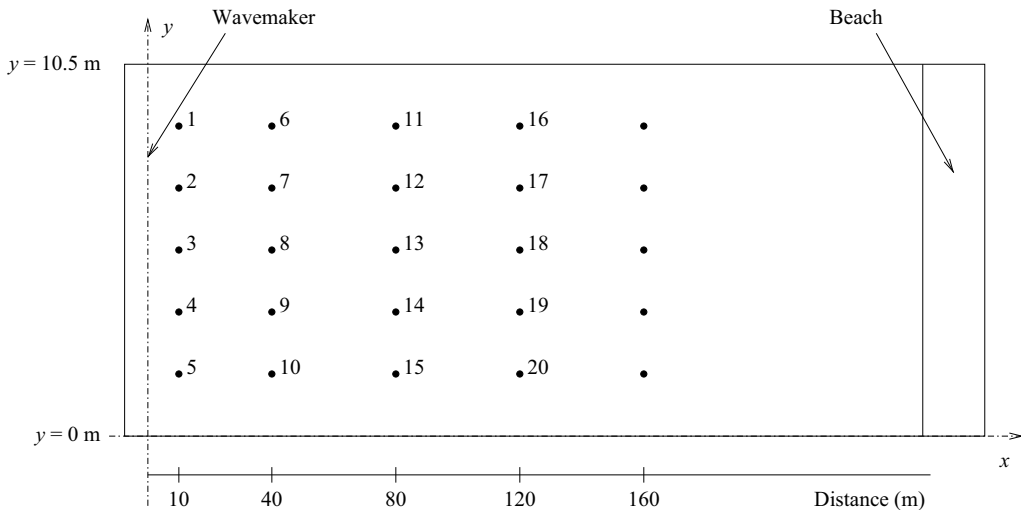


Figure 2. Experimental set-up with array of 20 probes. For runs 8000–8017 probes were located at  $x_1 = 10$ ,  $x_2 = 40$ ,  $x_3 = 80$  and  $x_4 = 120$  m. For runs 8018–8026 the probes and probe numbers at  $x = 40$ , 80 and 120 m were moved to 80, 120 and 160 m, respectively.

the 20 probes along and across the tank. A total of 27 experimental runs were carried out, of which four were repeated runs. Linear harmonic signals were used as input to the wave maker, i.e. the paddle oscillated like a single harmonic. As a result, free ‘parasitic’ overharmonic components will also propagate in the wave field at their own (much lower) speed, and be present after an additional time depending on the location. However, for the present study of modulations and downshift we do not consider that these effects disturb our findings, especially because time windows are chosen mostly before they arrive.

Table 1 gives a summary of the run numbers and the corresponding nominal period  $T$  and nominal wave height  $H$ . The nominal wave height is defined to be the peak-to-trough height of the generated uniform wave. We define the characteristic amplitude to be half the nominal wave height  $a_c = H/2$ , and we define the characteristic frequency to be given by the nominal period  $\omega_c = 2\pi/T$ . We let the characteristic wavenumber be given by the linear dispersion relation  $\omega_c^2 = gk_c \tanh k_c h$ , where  $g = 9.81 \text{ m s}^{-2}$  is the acceleration due to gravity and  $h$  is the depth. For all but runs 8004–8006 we can safely use the deep-water dispersion relation  $\omega_c^2 = gk_c$ . For this analysis we do not employ nonlinear corrections to the linear dispersion relation, leaving the nonlinear corrections to be taken care of by nonlinear evolution equations (e.g. Trulsen & Dysthe 1997). In the table we show the resulting values for the dimensionless depth  $k_c h$  and steepness  $\epsilon = a_c k_c$  for the shallower depth  $h = 5$  m. The transverse parameter  $\Delta\mu$  from (1.1) is also shown. The largest fetch  $\epsilon^2 k_c x_4$  is an important parameter telling us how long the tank is in terms of nonlinear modulational evolution. For ease of comparison we employ the same definition of fetch as in Trulsen & Dysthe (1997) inspired by the effect of cubic nonlinearities in the nonlinear Schrödinger equation. The last four columns of the table are explained in the next section.

The change of depth at 80 m from the wave maker does not have any impact on the results because we are in a deep-water regime. The results in Appendix A show that the interesting downshift happens after a longer propagation distance, which was the reason why we moved most of the probes to greater fetch for runs 8018–8026.

Runs 4–6 are test cases with large transverse parameter  $\Delta\mu$  and small fetch  $\epsilon^2 k_c x_4$ . They are not interesting and therefore not included in the following discussion.

Run	$T$ [s]	$H$ [m]	$k_c h$	$\epsilon$	$\Delta\mu$	$\epsilon^2 k_c x_4$	$\frac{\omega_{peak}(x_4)}{\omega_c}$	$\frac{\omega_{peak,c}(x_4)}{\omega_c}$	$\frac{\omega_{mean}(x_4)}{\omega_c}$	$\frac{\omega_{mean,c}(x_4)}{\omega_c}$
8000	1	0.05	20	0.1	0.074	4.9	1	1	1	1
8001	1	0.08	20	0.16	0.074	13	1	0.85	0.99	0.97
8002	1	0.1	20	0.2	0.074	20	0.81	0.81	0.92	0.91
8003	1	0.13	20	0.26	0.074	33	0.73	0.75	0.88	0.87
8004	2.5	0.1	3.2	0.032	0.46	0.08	0.98	0.98	0.98	0.98
8005	2	0.1	5	0.05	0.3	0.31	0.98	0.98	0.98	0.98
8006	3	0.1	2.2	0.022	0.67	0.027	1	1	1	1
8007	0.82	0.04	30	0.12	0.05	10	1	1	1	0.99
8008	0.82	0.06	30	0.18	0.05	23	0.82	0.83	0.92	0.92
8009	1.24	0.11	13	0.14	0.11	6.5	1	1	1	1
8010	1.24	0.15	13	0.2	0.11	12	1	1	1	1
8011	1.24	0.19	13	0.25	0.11	19	0.8	0.8	0.94	0.92
8012	1.24	0.24	13	0.31	0.11	31	1	1	0.95	0.91
8013	1	0.16	20	0.32	0.074	50	0.73	0.73	0.87	0.86
8014	0.82	0.03	30	0.09	0.05	5.8	1	1	1	1
8015	0.82	0.04	30	0.12	0.05	10	1	0.89	1	1
8016	0.82	0.05	30	0.15	0.05	16	0.85	0.85	0.97	0.95
8017	0.82	0.08	30	0.24	0.05	41	0.74	0.74	0.88	0.87
8018	1	0.03	20	0.06	0.074	2.3	1	1	1	1
8019	1	0.08	20	0.16	0.074	17	0.85	0.85	0.96	0.94
8020	1.43	0.15	9.8	0.15	0.15	6.9	1	1	1	1
8021	1.43	0.2	9.8	0.2	0.15	12	1	1	1	1
8022	1.43	0.25	9.8	0.25	0.15	19	1	1	0.96	0.94
8023	1.43	0.31	9.8	0.31	0.15	29	1	1	0.96	0.95
8024	1.43	0.225	9.8	0.22	0.15	15	1	1	1	0.99
8025	1.43	0.31	9.8	0.31	0.15	29	1	1	0.96	0.96
8026	1	0.1	20	0.2	0.074	26	0.8	0.8	0.9	0.9

Table 1. First column run number. Next six columns nominal parameter values: period, wave height, dimensionless depth (for the shallower depth  $h = 5$  m), steepness, width parameter, largest fetch. Final four columns downshift at largest fetch: peak across tank, peak at centreline, mean across tank, mean at centreline.

### 3. Data analysis

The  $x$ -axis is along the tank, the  $y$ -axis is across and the  $z$ -axis is vertical pointing up. The surface elevation is  $z = \eta$  with quiescent surface  $z = 0$ . The velocity field is  $\mathbf{v} = \nabla\phi$  according to an assumption of potential flow.

At the lateral vertical walls there is no flow through the walls  $v_y = 0$ . In the case of gravity waves and potential flow, the normal derivative of the surface elevation vanishes at the walls,  $\partial\eta/\partial y = 0$ . This can be established from the exact dynamic surface condition

$$\frac{\partial\phi}{\partial t} + g\eta + \frac{1}{2}(\nabla\phi)^2 = 0 \quad \text{at } z = \eta. \quad (3.1)$$

Upon taking the  $y$ -derivative and evaluating at the lateral wall we get the desired result.

In the following we outline a Fourier analysis in the transverse ( $y$ ) and time ( $t$ ) domains, with no Fourier decomposition in the longitudinal ( $x$ ) direction.

Having established that  $\partial\eta/\partial y = 0$  at the lateral walls, we can represent the transverse behaviour of the surface elevation by an infinite cosine series

$$\eta(x, y, t) = \sum_{n=0}^{\infty} \tilde{\eta}_n(x, t) \cos\left(\frac{\pi n y}{b}\right). \quad (3.2)$$

We proceed as in Trulsen *et al.* (1999), but now truncating (3.2) to the first five terms, insisting on exact reproduction at the collocation points

$$\eta(x, y_l, t) = \sum_{n=0}^4 \check{\eta}_n(x, t) \cos\left(\frac{\pi n y_l}{b}\right) \quad \text{for } l = 1, 2, 3, 4, 5. \quad (3.3)$$

With  $y_l/b = l/6$  the coefficients are obtained by the transform

$$\begin{pmatrix} \check{\eta}_0 \\ \check{\eta}_1 \\ \check{\eta}_2 \\ \check{\eta}_3 \\ \check{\eta}_4 \end{pmatrix} = \frac{1}{6} \begin{pmatrix} 2 & 0 & 2 & 0 & 2 \\ 2\sqrt{3} & 0 & 0 & 0 & -2\sqrt{3} \\ 3 & -3 & 0 & -3 & 3 \\ \sqrt{3} & -3 & 0 & 3 & -\sqrt{3} \\ 1 & -3 & 4 & -3 & 1 \end{pmatrix} \begin{pmatrix} \eta(y_1) \\ \eta(y_2) \\ \eta(y_3) \\ \eta(y_4) \\ \eta(y_5) \end{pmatrix}. \quad (3.4)$$

In the following, we use the truncated (3.3) as the basis for interpolation across the tank

$$\eta(x, y, t) = \sum_{n=0}^4 \check{\eta}_n(x, t) \cos\left(\frac{\pi n y}{b}\right). \quad (3.5)$$

We take the temporal Fourier transform over a time interval  $\tau$  starting at an offset time depending on the position  $\tau_0(x)$

$$\check{\eta}_n(x, t) = \sum_j \hat{\eta}_{n,j}(x) e^{-i\omega_j t} \quad \text{for } \tau_0(x) \leq t < \tau_0(x) + \tau, \quad (3.6)$$

where  $\omega_j = 2\pi j/\tau$ . The offset starting time  $\tau_0(x)$  serves two purposes. First,  $\tau_0(x)$  is chosen large enough that all startup effects have disappeared. Second,  $d\tau_0/dx = c_g$  in order to recognise that energy is transported with the group velocity. Between two positions  $x_1$  and  $x_2$  we have  $x_1 - x_2 = c_g(\tau_0(x_1) - \tau_0(x_2))$ , where  $c_g$  is the group velocity corresponding to the nominal wave period  $T$ .

With the advantage of the orthogonality of the interpolating functions, we can now compute the mean power in the combined time and transverse domain

$$I(x) = \frac{1}{\tau} \int_{\tau_0(x)}^{\tau_0(x)+\tau} \frac{1}{b} \int_0^b \eta^2(x, y, t) dy dt = \sum_j \sum_{n=0}^4 v_n |\hat{\eta}_{n,j}(x)|^2, \quad (3.7)$$

where we have introduced the coefficient  $v_n$  such that  $v_0 = 1$  and  $v_n = 1/2$  for  $n > 0$ .

Introducing the power of each mode

$$J_n(x, \omega_j) = v_n |\hat{\eta}_{n,j}(x)|^2, \quad (3.8)$$

the transversally integrated power

$$F(x, \omega_j) = \sum_{n=0}^4 J_n(x, \omega_j), \quad (3.9)$$

and the temporally integrated power

$$G_n(x) = \sum_j J_n(x, \omega_j), \quad (3.10)$$



we have that the total mean power is

$$I(x) = \sum_{n=0}^4 G_n(x) = \sum_j F(x, \omega_j) = \sum_j \sum_{n=0}^4 J_n(x, \omega_j). \quad (3.11)$$

Sometimes experiments are carried out with only one probe across the tank for each longitudinal position  $x$ ; typically, such probes are located along the centreline of the tank. In our case this corresponds to transverse position  $y_3 = b/2$  and we define  $\zeta(x, t) \equiv \eta(x, y_3, t) = \check{\eta}_0(x, t) - \check{\eta}_2(x, t) + \check{\eta}_4(x, t)$ , where we have employed the interpolation formula (3.5). Again we take the temporal Fourier transform over a time interval  $\tau$  starting at an offset time depending on position  $\tau_0(x)$

$$\zeta(x, t) \equiv \eta(x, y_3, t) = \sum_j \hat{\zeta}_j(x) e^{-i\omega_j t} \quad \text{for } \tau_0(x) \leq t < \tau_0(x) + \tau, \quad (3.12)$$

from which we identify the mean power in the time domain

$$C(x) = \frac{1}{\tau} \int_{\tau_0(x)}^{\tau_0(x)+\tau} \eta^2(x, y_3, t) dt = \sum_j |\hat{\zeta}_j(x)|^2 = \sum_j D(x, \omega_j), \quad (3.13)$$

where  $D(x, \omega_j) = |\hat{\zeta}_j(x)|^2$ .

We have computed three different kinds of peak frequencies of the power spectrum: The peak frequency of each transverse mode  $\omega_{peak,n}(x)$  is the frequency  $\omega_j$  that maximises  $J_n(x, \omega_j)$  for each  $n \in \{0, 1, 2, 3, 4\}$ . The peak frequency for the combined measurements across the tank  $\omega_{peak}(x)$  is the frequency  $\omega_j$  that maximises  $F(x, \omega_j)$ . The peak frequency at the centreline of the tank  $\omega_{peak,c}(x)$  is the frequency  $\omega_j$  that maximises  $D(x, \omega_j)$ .

For all of the peak frequencies, we limit the search to a frequency range strictly within the first harmonic domain  $\delta < \omega_{peak}/\omega_c < 2 - \delta$ , where  $\delta$  is a small number.

Similarly, we have computed three different kinds of mean frequencies of the power spectrum: the mean frequency of each transverse mode is

$$\omega_{mean,n}(x) = \sum_j |\omega_j| J_n(x, \omega_j) / G_n(x). \quad (3.14)$$

The mean frequency for the combined measurements across the tank is

$$\omega_{mean}(x) = \sum_j |\omega_j| F(x, \omega_j) / I(x). \quad (3.15)$$

The mean frequency at the centreline of the tank is

$$\omega_{mean,c}(x) = \sum_j |\omega_j| D(x, \omega_j) / C(x). \quad (3.16)$$

The evolution of these quantities along the tank is expected to be dominated by cubic nonlinear interactions, e.g. described by the nonlinear Schrödinger equation, therefore we have chosen to normalise the evolution  $x$ -axis by the square of the nominal steepness  $\epsilon$  (Trulsen & Dysthe 1997).

#### 4. Results

Here, we give detailed results for run 8019. Detailed results for all runs can be found in [Appendix A](#). Pictures from the runs can be found in [Appendix B](#).

Quantity	Explanation
$J_n(x, \omega_j)$	Power of each transverse mode $n$ and frequency $\omega_j$
$F(x, \omega_j)$	Transversally integrated power of each frequency $\omega_j$
$G_n(x)$	Temporally integrated power of each transverse mode $n$
$I(x)$	Temporally and transversally integrated power
$D(x, \omega_j)$	Power at centreline of each frequency $\omega_j$
$C(x)$	Temporally integrated power at centreline

Table 2. Summary of quantities presented.

In order to help the interpretation of the following figures we offer [table 2](#) with a summary of the quantities that are being presented.

[Figure 3](#) shows the frequency power spectrum  $J_n(x, \omega)$  for each transverse mode number  $n$  at each station  $x$ , normalised such that the peak value is 1 at each station  $x$ . Two different views are shown: to the left, spectral curves as a function of  $\omega$  for each value of  $n$ ; to the right, intensity plots in the  $(\omega, n)$ -plane. Notice that  $\omega$  increases to the right in the left column while it increases downward in the right column. We observe significant downshift of the peak frequency, and a certain amount of energy transfer to transverse modes  $n > 0$ . The long-crested mode  $n = 0$  and the first transverse mode  $n = 1$  have significantly downshifted peaks, while all modes have significant energy leakage to higher frequencies. All figures are limited to the first harmonic frequency domain  $0 < \omega < 2\omega_c$ .

[Figure 4](#) shows the mean power of each transverse mode  $G_n(x)$ , the total mean power  $I(x)$  and the mean power along the centreline of the tank  $C(x)$ . If we limit consideration to only the centreline, or only the long-crested part of the wave  $n = 0$ , then we may overestimate the amount of dissipation. A significant portion of the energy is transferred to transverse modes  $n > 0$ .

Both [figures 3](#) and [4](#) imply that a significant amount of energy can be transferred to transverse modes, and thus dissipation can be overestimated by just observing the long-crested mode or just measuring at the centreline. These two figures also suggest that the main contributions to the energy budget can be captured by just considering the long-crested mode  $n = 0$  and the first transverse mode  $n = 1$ .

[Figure 5](#) shows the peak and mean frequencies. To the left we see the peak frequency  $\omega_{peak,n}(x)$  for each transverse mode  $J_n(x, \omega)$ , the peak frequency  $\omega_{peak}(x)$  for the combined measurements across the tank  $F(x, \omega)$  and the peak frequency  $\omega_{peak,c}(x)$  at the centreline of the tank  $D(x, \omega)$ . To the right we see the mean frequency  $\omega_{mean,n}(x)$  for each transverse mode  $J_n(x, \omega)$ , the mean frequency  $\omega_{mean}(x)$  for the combined measurements across the tank  $F(x, \omega)$  and the mean frequency  $\omega_{mean,c}(x)$  at the centreline of the tank  $D(x, \omega)$ . Several of the transverse modes  $n > 0$  may actually experience significant upshift, but they do not carry significant amount of energy, therefore there is a clear tendency of downshift for the wave system as a whole and along the centreline.

## 5. Discussion

The results can be summarised in parametric  $(\epsilon, \Delta\mu)$ -plots in order to distinguish which parametric regimes that give downshift. [Figure 6](#) shows results for the downshift of the peak frequency  $\omega_{peak}(x)$ , while [figure 7](#) shows results for the downshift of the mean frequency  $\omega_{mean}(x)$ , in both cases for the combined measurements across the tank  $F(x, \omega)$ . Each run corresponds to a cross,  $\times$ , or a cross in a circle,  $\otimes$ .

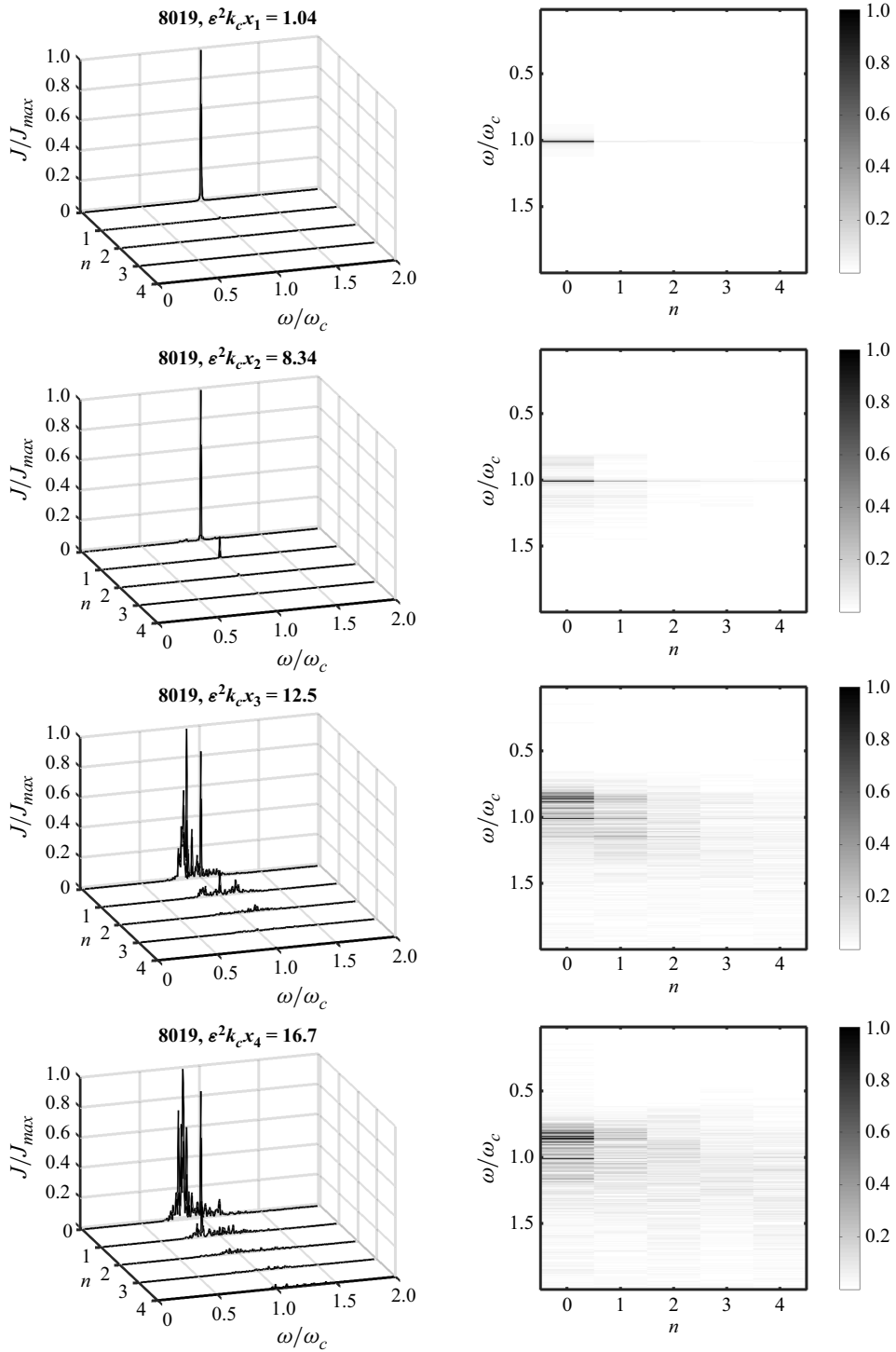


Figure 3. Frequency power spectrum  $J_n(x, \omega)$  for each transverse mode number  $n$  at each station  $x$ , normalised such that the peak value is 1 at each station  $x$ .

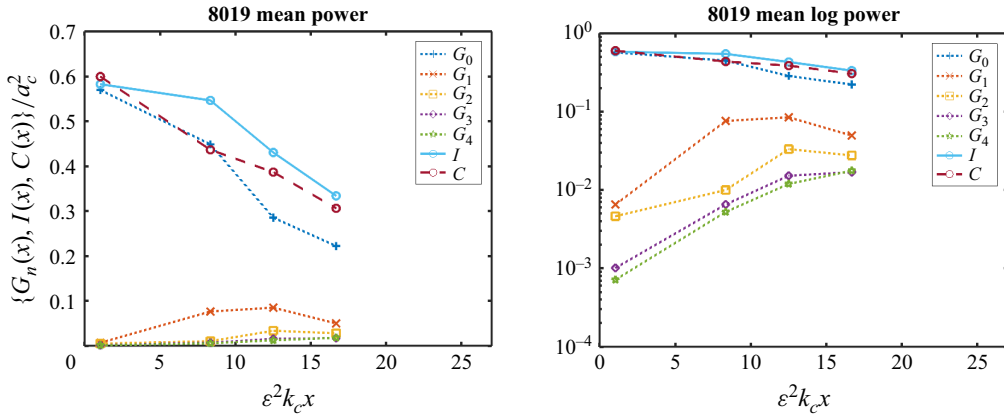


Figure 4. Mean power along the tank for each transverse mode  $G_n(x)$ , the total mean power  $I(x)$  and the mean power along the centreline of the tank  $C(x)$ . Linear and logarithmic power axes. Each set of four discrete points is connected with straight lines (linear interpolation).

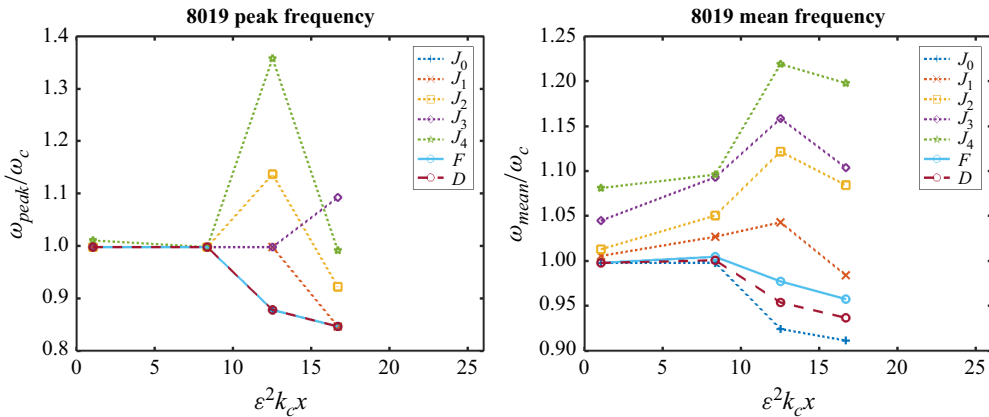


Figure 5. Peak and mean frequencies along the tank,  $\omega_{peak,n}(x)$  and  $\omega_{mean,n}(x)$  for each transverse mode  $J_n(x, \omega)$ ,  $\omega_{peak}(x)$  and  $\omega_{mean}(x)$  for the combined measurements across the tank  $F(x, \omega)$ ,  $\omega_{peak,c}(x)$  and  $\omega_{mean,c}(x)$  for the centreline of the tank  $D(x, \omega)$ . Each set of four discrete points is connected with straight lines (linear interpolation).

Colours indicate the amount of downshift at the last probe location  $x_4$ . For the duplicate runs with identical parameter values ( $\epsilon$ ,  $\Delta\mu$ ), only the highest run numbers with the largest value of  $x_4$  were employed in order to compute the contour levels. Runs with the largest amount of downshift are shown in blue. Runs with smaller amounts of downshift are shown in red. Runs without downshift or with little downshift are shown in black. The chosen contour levels are different for the peak frequency in figure 6 and for the mean frequency in figure 7, and are given in the figure captions, because the peak frequency downshift is larger than the mean frequency downshift.

In these plots the solid contours are obtained from the irregular grid of data points using the ‘griddata’ command in Octave/Matlab with linear interpolation. We have attempted to parameterise the experimental result by the formulas  $\Delta\mu = 0.2(\epsilon - 0.15)^{0.25}$  shown in red dots and  $\Delta\mu = 0.1(\epsilon - 0.22)^{0.1}$  shown in blue dots.

Run numbers 2 and 26 both correspond to the single experiment reported in Trulsen *et al.* (1999). We confirm that this choice of ( $\epsilon$ ,  $\Delta\mu$ ) indeed produces a downshift, as

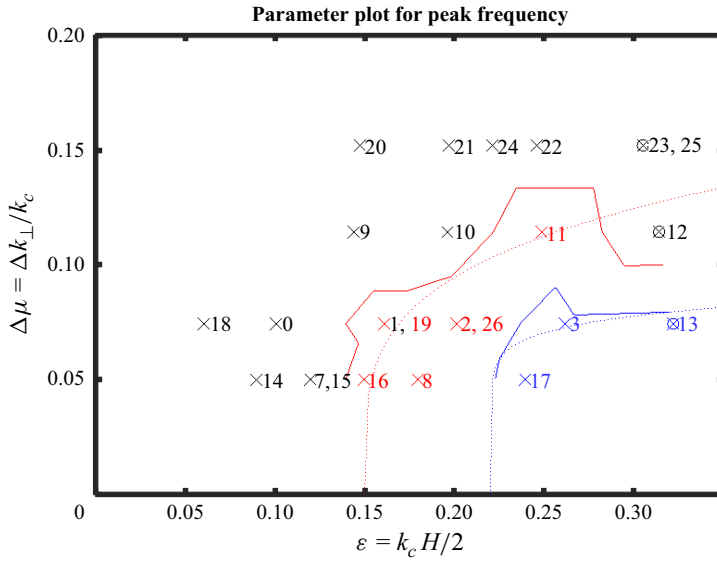


Figure 6. Parametric plot for peak frequency downshift. Runs without,  $\times$ , and with,  $\otimes$ , clear visual observation of type II horseshoe patterns. Run numbers reduced by 8000. Colours: black, no downshift  $\Delta\omega_{peak}/\omega_c > 0.9$ ; red, small downshift  $0.9 \geq \Delta\omega_{peak}/\omega_c > 0.76$ ; blue, clear downshift  $\Delta\omega_{peak}/\omega_c \leq 0.76$ . Solid red contour at value 0.9, solid blue contour at value 0.76. Dotted contours attempted parameterisation explained in text.

previously reported. The fact that run number 10, with equal steepness  $\epsilon$  and greater  $\Delta\mu$ , does not produce a downshift suggests that transverse modulations are essential for this downshift to occur.

Run 11 has downshift while run 10 does not. They have the same value of  $\Delta\mu$ , but run 11 has greater steepness  $\epsilon$  than run 10. This is likely associated with the greater amount of energy loss in the steeper run 11, possibly giving support to previous findings that damping associated with heavy modulations can give downshift for long-crested waves (e.g. Trulsen & Dysthe 1990).

Run 19 has downshift while run 1 does not, for the same values of  $(\epsilon, \Delta\mu)$ . This is due to the probes being too close to the wave maker for run 1. The probes were moved farther down the tank for runs 8018–8026. We employed the result from run 8019 in order to draw the solid contour curves.

Experimental runs with clear visual observation of type II horseshoe patterns are indicated by circles with crosses  $\otimes$ , this happens for the largest values of steepness  $\epsilon > 0.3$ . The results clearly show that the downshift does not depend on type II modulational instability or the horseshoe modulation pattern. It is interesting to note that run 12 does not have a clear downshift of the peak frequency, while run 11 does, suggesting that the downshift depends on type I rather than type II modulational instability.

The downshift clearly depends on the combination of the tank being sufficiently wide and the wave being sufficiently steep. The thresholds are approximately  $\Delta\mu \approx 0.1$  and  $\epsilon \approx 0.15$ . Downshift can happen in wide wave tanks  $\Delta\mu < 0.1$  for steepness  $\epsilon > 0.15$ . For narrower wave tanks  $0.1 < \Delta\mu < 0.12$ , downshift can happen for larger steepness  $\epsilon \approx 0.25$ , but it is not clear that an even greater steepness  $\epsilon > 0.3$  will guarantee downshift for these values of  $\Delta\mu$ . For even narrower wave tanks  $\Delta\mu > 0.12$  it is not clear that a downshift can happen regardless of the steepness.

Those runs with the largest steepness denoted by circle and cross,  $\otimes$ , correspond to clear observations of type II broad-band horseshoe patterns along the wave crests. Not all of the



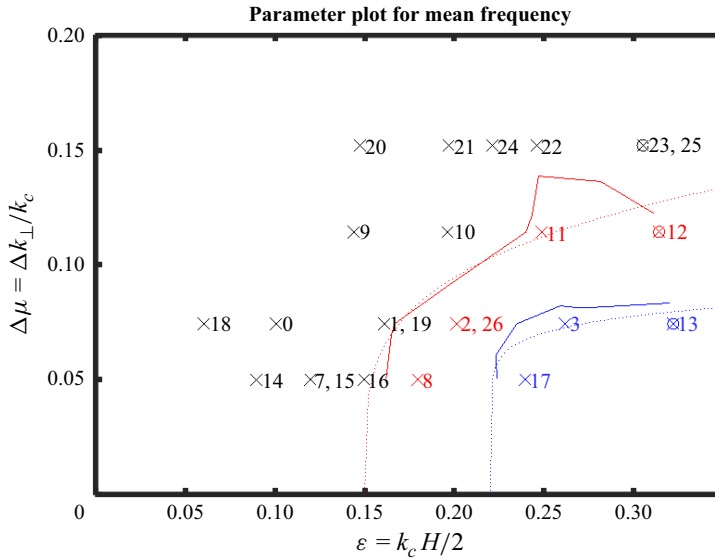


Figure 7. Parametric plot for mean frequency downshift. Runs without,  $\times$ , and with,  $\otimes$ , clear visual observation of type II horseshoe patterns. Run numbers reduced by 8000. Colours: black, no downshift  $\Delta\omega_{\text{mean}}/\omega_c > 0.95$ ; red, small downshift  $0.95 \geq \Delta\omega_{\text{mean}}/\omega_c > 0.89$ ; blue, clear downshift  $\Delta\omega_{\text{mean}}/\omega_c \leq 0.89$ . Solid red contour at value 0.95, solid blue contour at value 0.89. Dotted contours attempted parameterisation explained in text.

cases with horseshoe patterns did show downshift, only those with sufficiently small  $\Delta\mu$  showed downshift. We therefore do not expect that type II modulations play any role in the frequency downshift.

The detailed results in [Appendix A](#) clearly show that if measurements were limited to only the centreline along the tank, with only one probe across the tank, the conclusions would have been different from those discussed above. This could have resulted in an overestimation of the energy dissipation and an incorrect estimation of the frequency downshift. This is because energy and frequency content can be ‘hidden’ in the transverse modes. Our results suggest that it may be sufficient to include only the first transverse mode  $n = 1$  in addition to the long-crested mode  $n = 0$ , this should be investigated with appropriate models in the future.

Pictures from all the experiments are shown in [Appendix B](#).

The most significant limitation of these experiments is the rather limited maximum normalised evolution distance  $\epsilon^2 k_c x_4$ , possibly concealing downshift at greater distances for some of the runs.

Comparing these results with previous literature, we should keep in mind that many previous investigations on downshift were done with seeded waves, while our experiments employ unseeded waves.

While the most accepted paradigms for downshifting argue that dissipation is required for downshifting to occur. Our experiments contain both dissipation and transverse modulation at the same time. The full explanation for downshifting likely depends on both.

## 6. Conclusions

We have presented experimental evidence for the numerical prediction of Trulsen & Dysthe (1997), confirming and extending the experimental observation of Trulsen

*et al.* (1999), that transverse narrow-banded modulations can play an essential role in the evolution of initially uniform long-crested waves, and can facilitate a frequency downshift. Insufficient measurement resolution across the tank can result in overestimating dissipation and incorrect estimation of the amount of downshifting, because energy and frequency content can be ‘hidden’ in transverse modes. We observe clear downshift only in cases that allow significant interactions with unstable narrow-banded transverse modes, corresponding to transverse type I instability. We do not necessarily observe downshift with modulations of unstable wide-banded transverse modes, corresponding to type II instability. A criterion for downshift appears to be that the wave tank should accommodate crest lengths of at least 10 wavelengths.

**Funding.** This work was initiated in 1997 as a collaboration between Kristian B. Dysthe at the University of Bergen, Carl Trygve Stansberg at Marintek and Karsten Trulsen first at the University of Bergen and then at Universidad Complutense de Madrid. The experiments were carried out at Marintek in 1998. Kristian B. Dysthe died 30 July 2023, before the paper was finished. The analysis and writing was completed by Karsten Trulsen at the University of Oslo. The experiments were funded by Norsk Hydro. We thank Gunnar Furnes, then at Norsk Hydro, for his support securing that funding. The early stage of this work was supported by the Research Council of Norway grant RCN 109382 and the European Union grant MAS3-CT96-5016.

**Declaration of interests.** The authors report no conflict of interest.

## Appendix A. Detailed analysis for each run

Figures 8–31 show detailed analysis of the various experimental runs. For explanation please see the legends of figures 3–5.

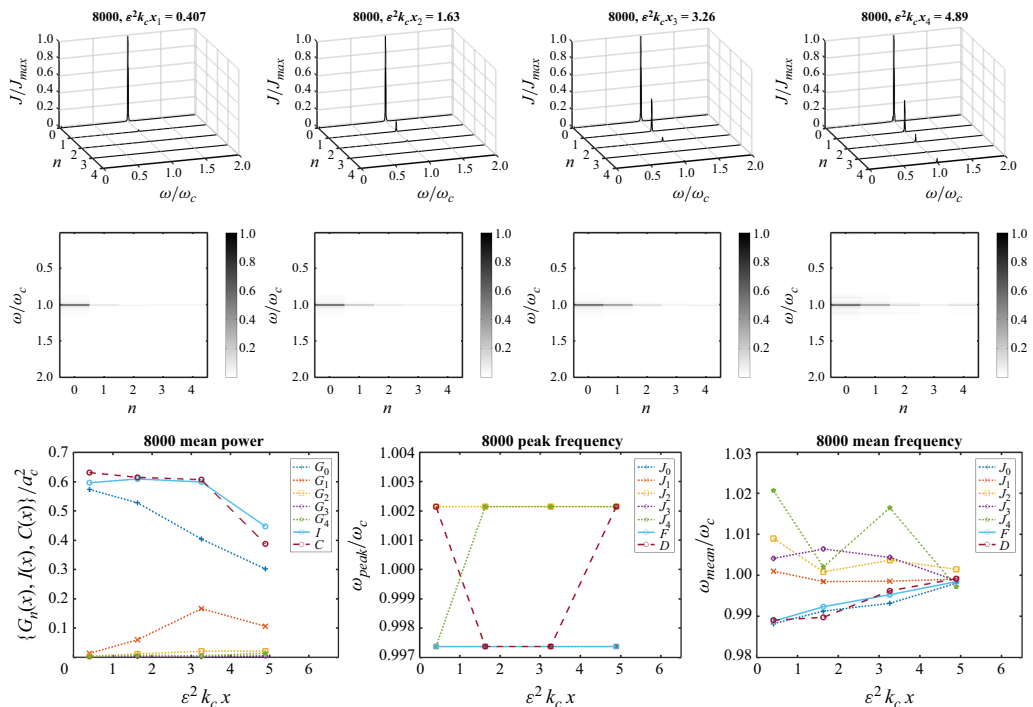


Figure 8. Run 8000.

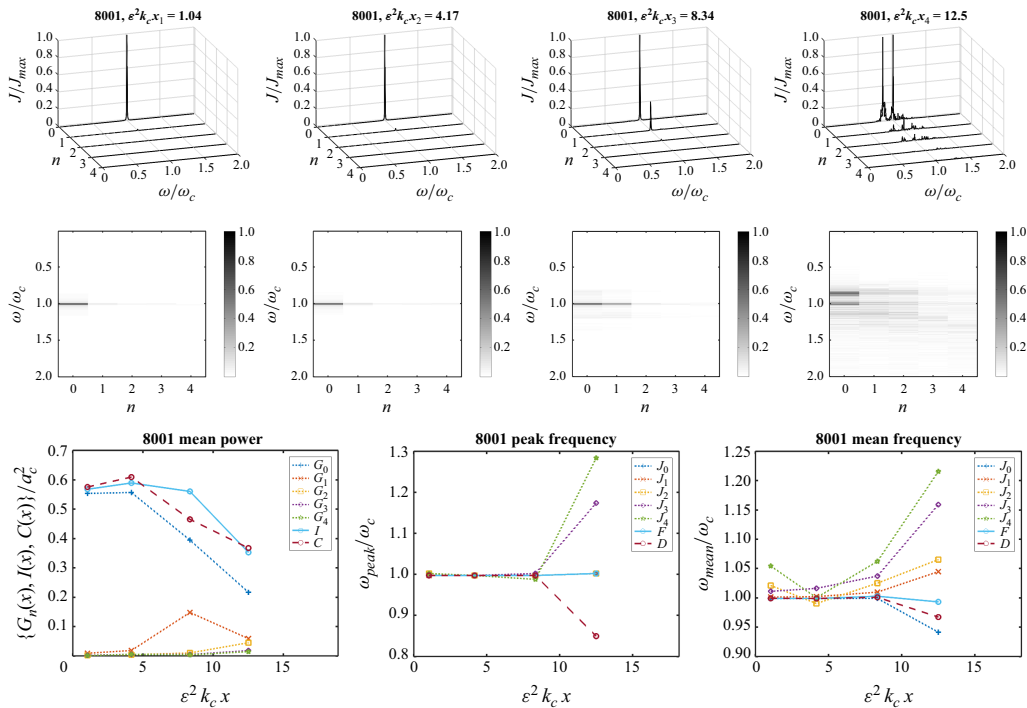


Figure 9. Run 8001.

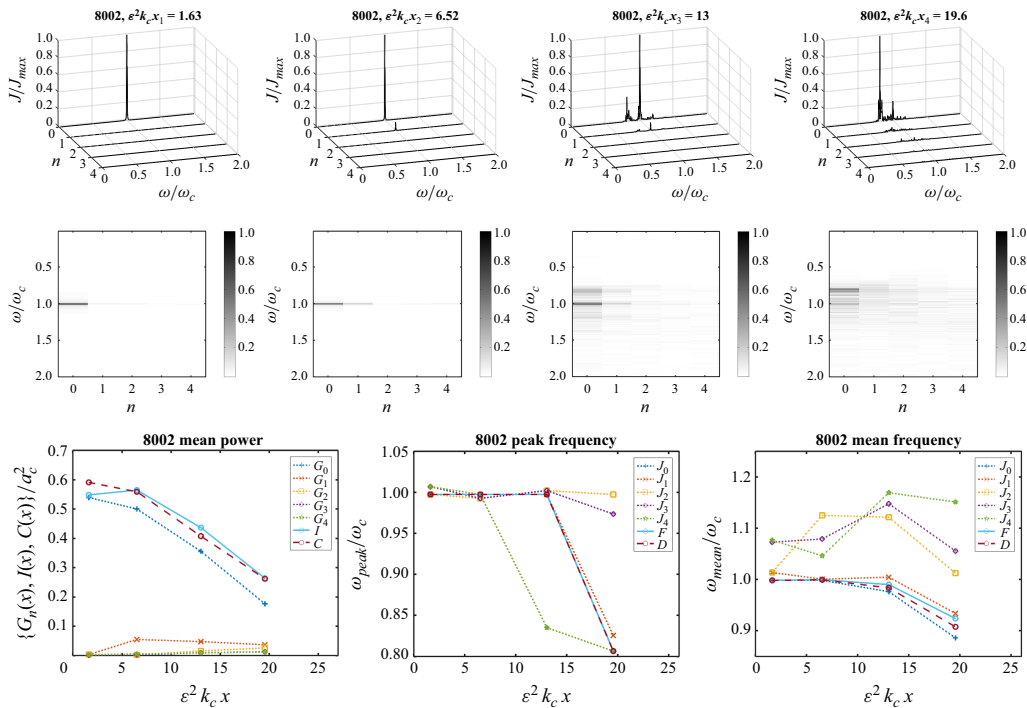


Figure 10. Run 8002.

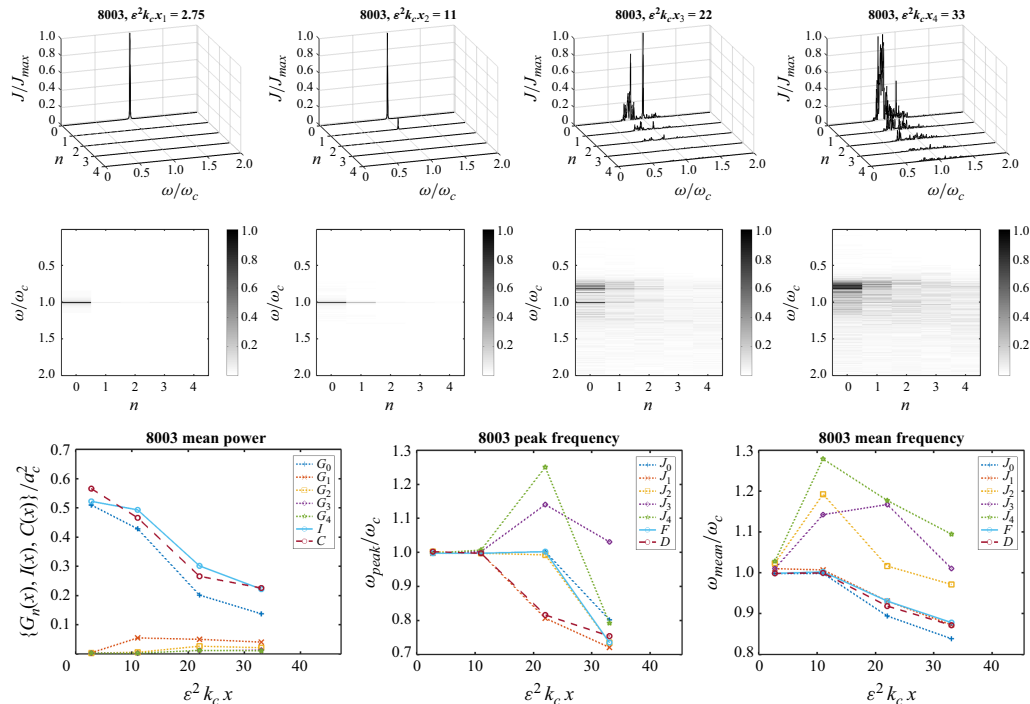


Figure 11. Run 8003.

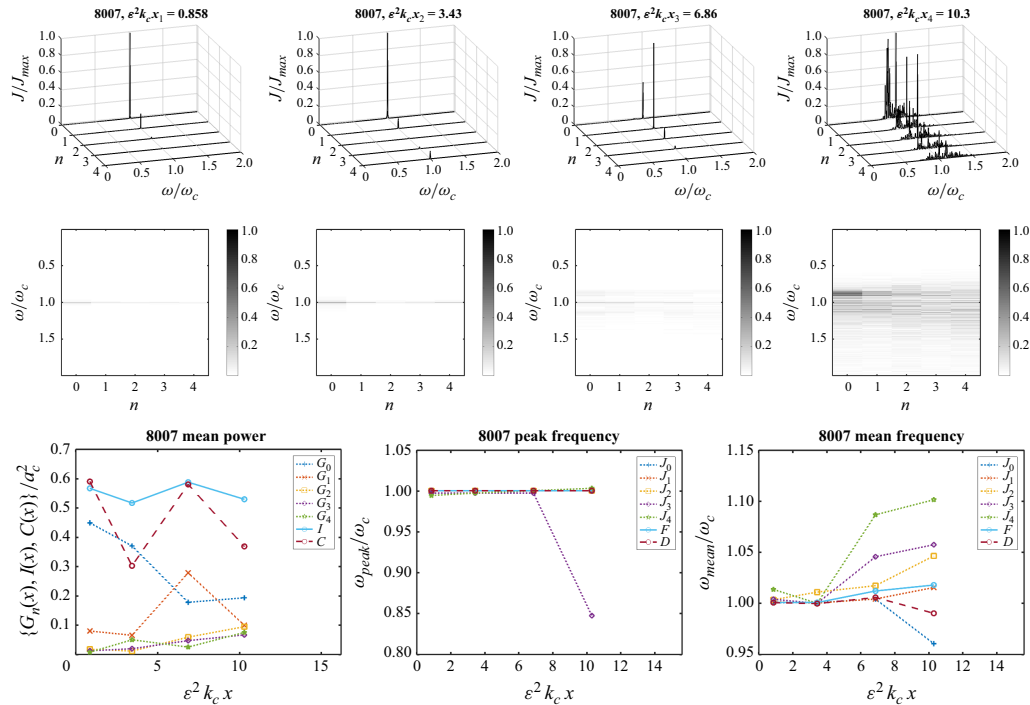
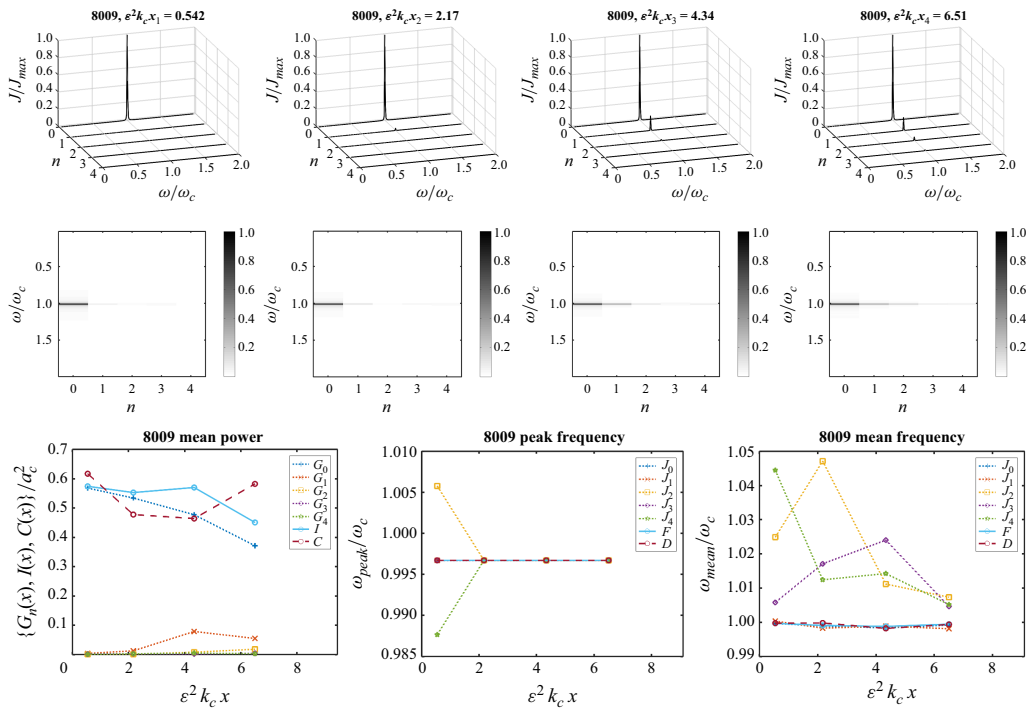
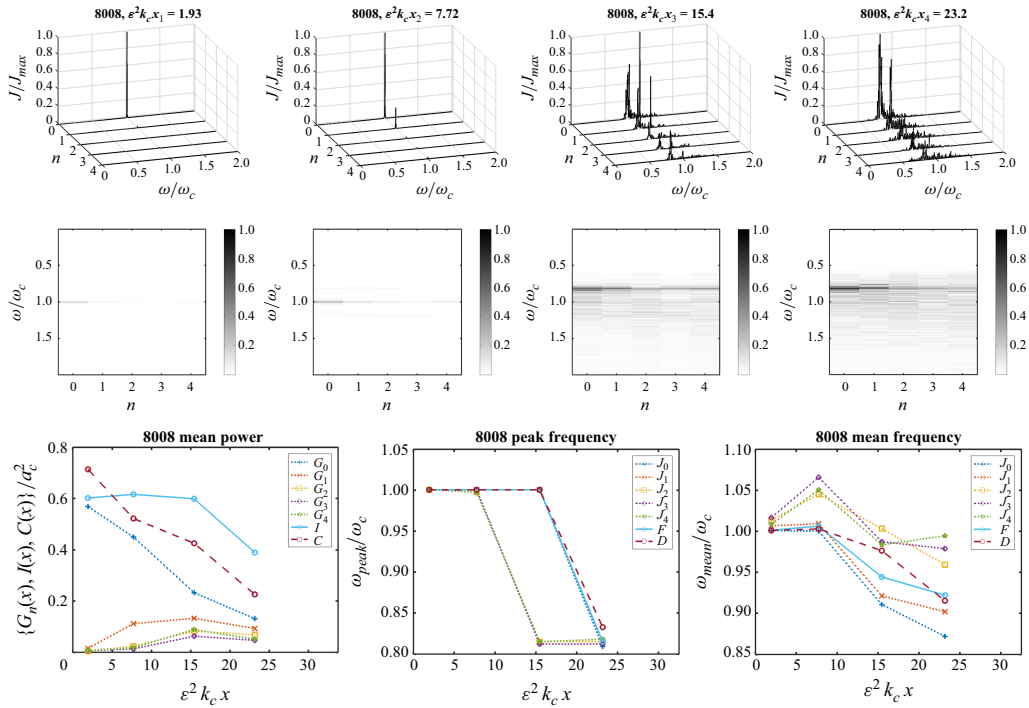


Figure 12. Run 8007.





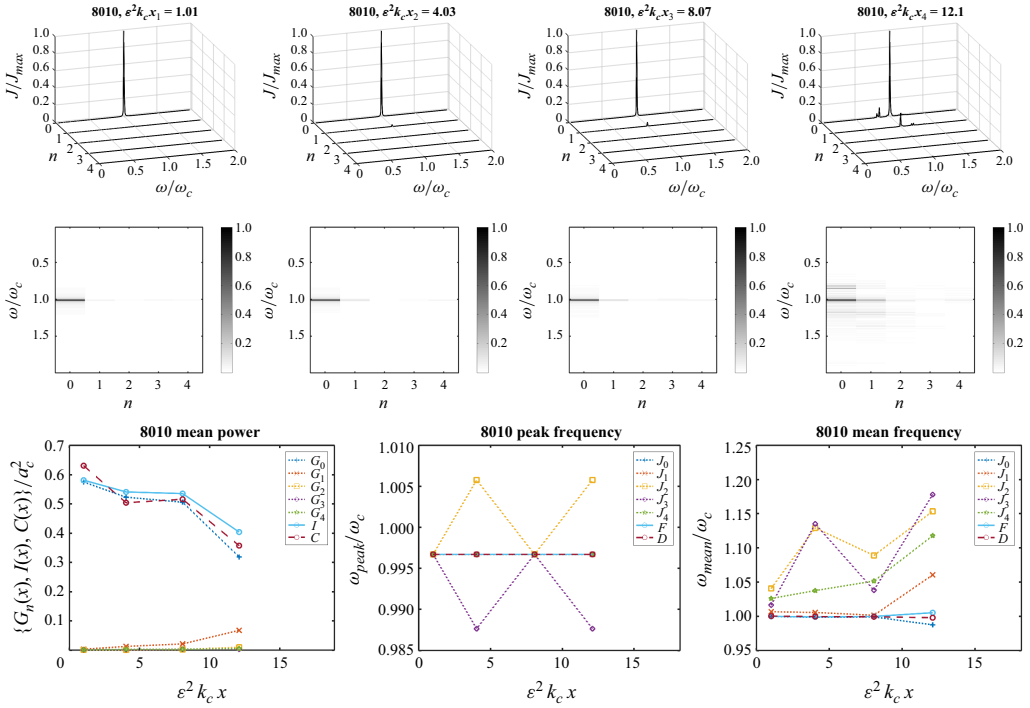


Figure 15. Run 8010.

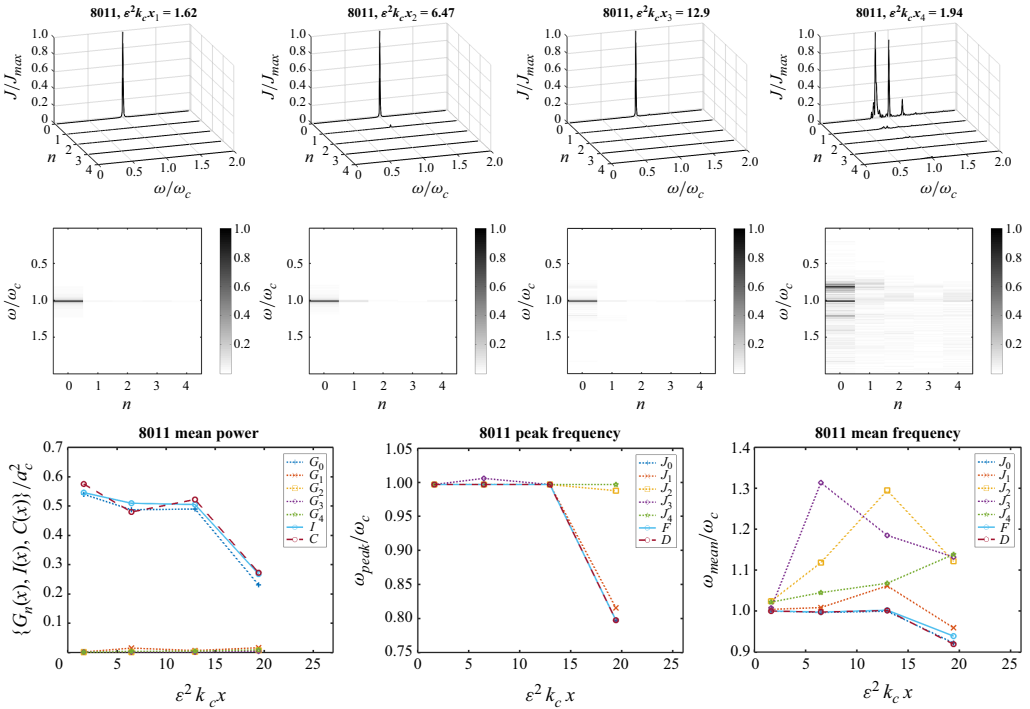


Figure 16. Run 8011.

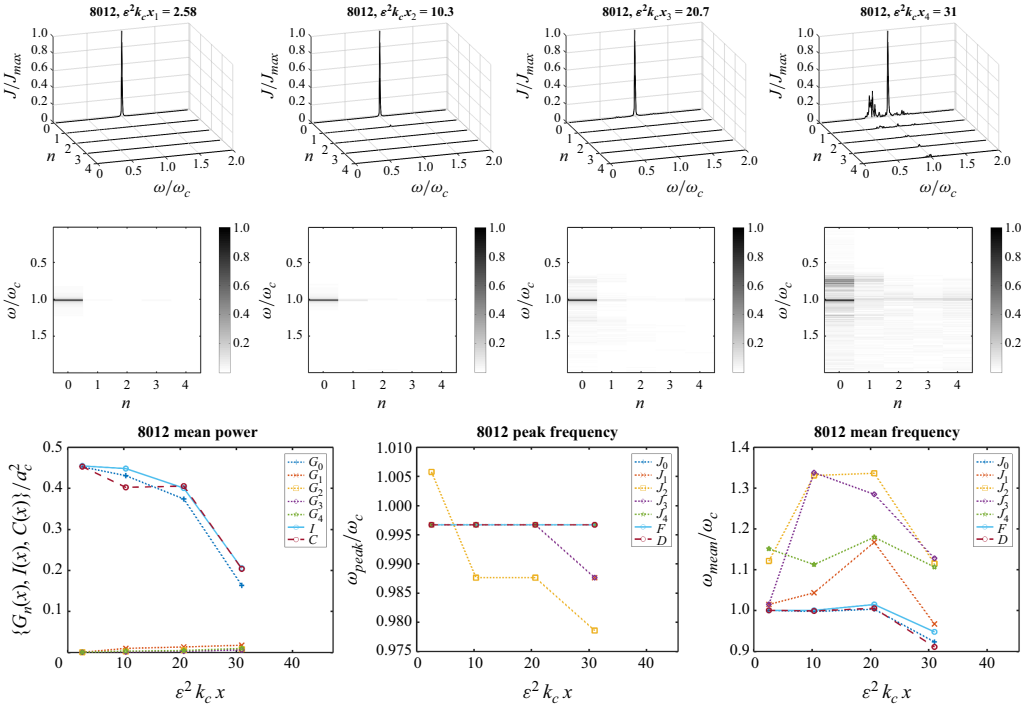


Figure 17. Run 8012.

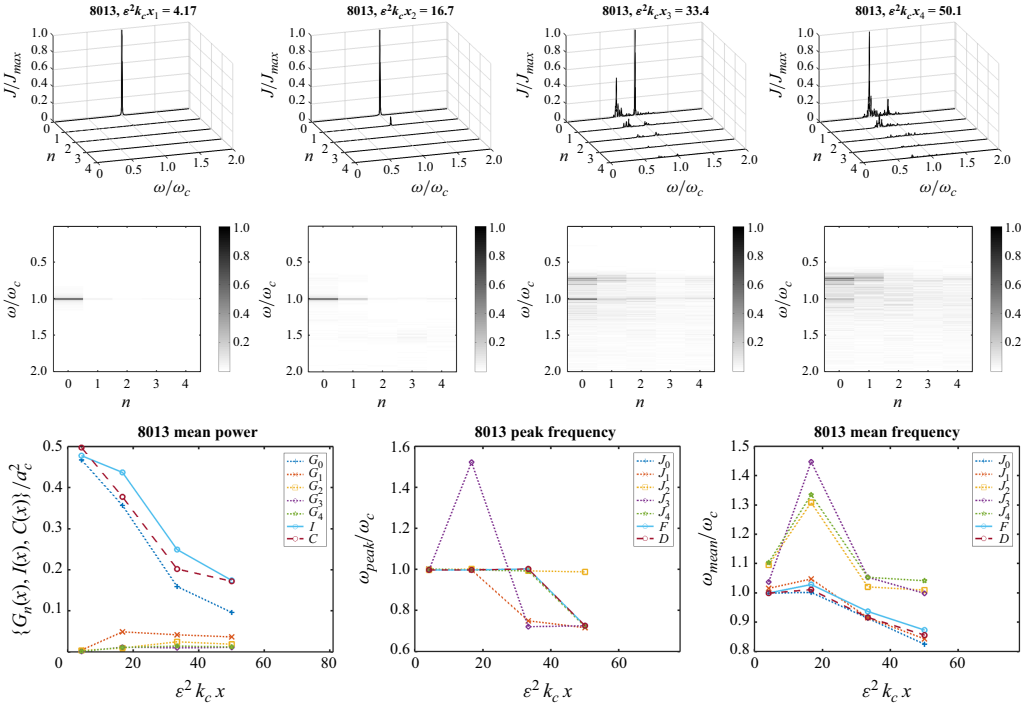


Figure 18. Run 8013.

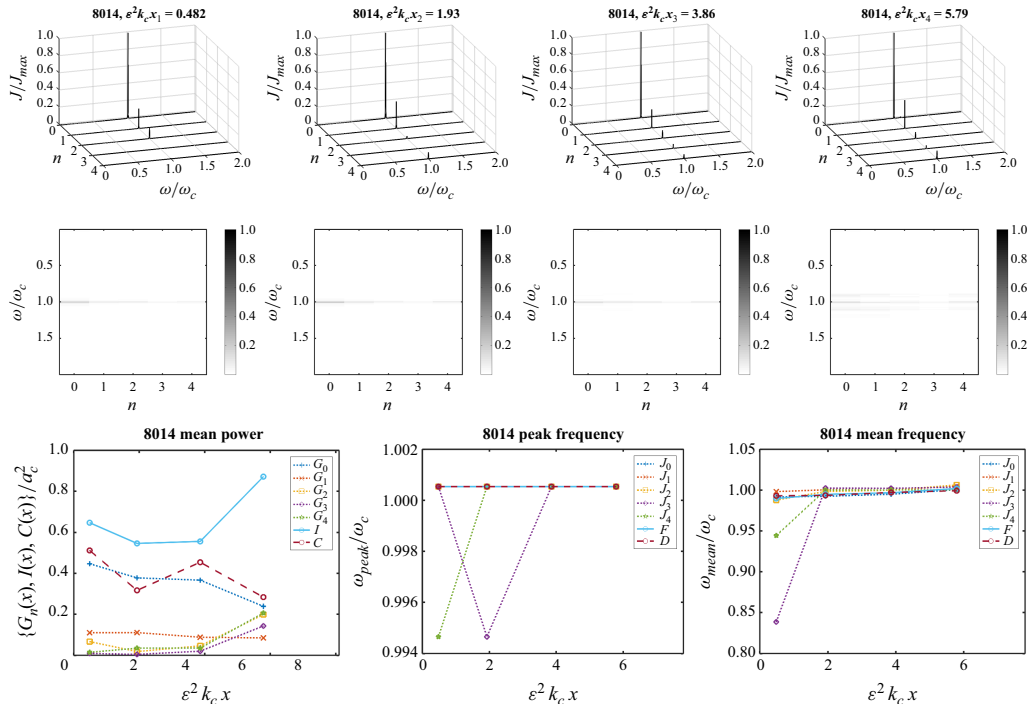


Figure 19. Run 8014.

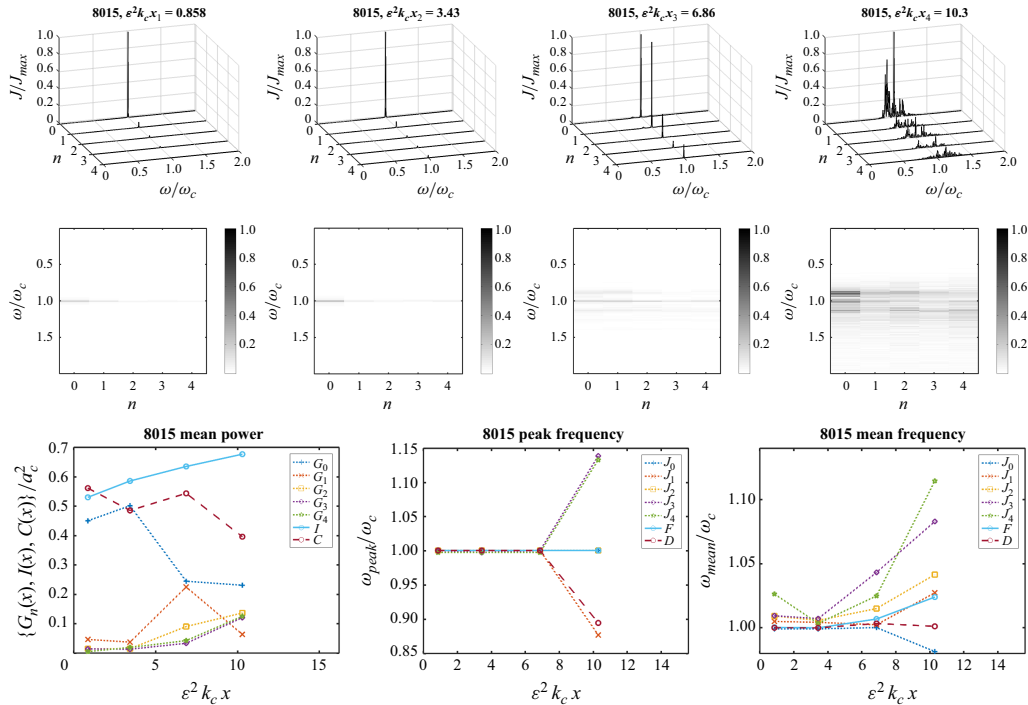


Figure 20. Run 8015.

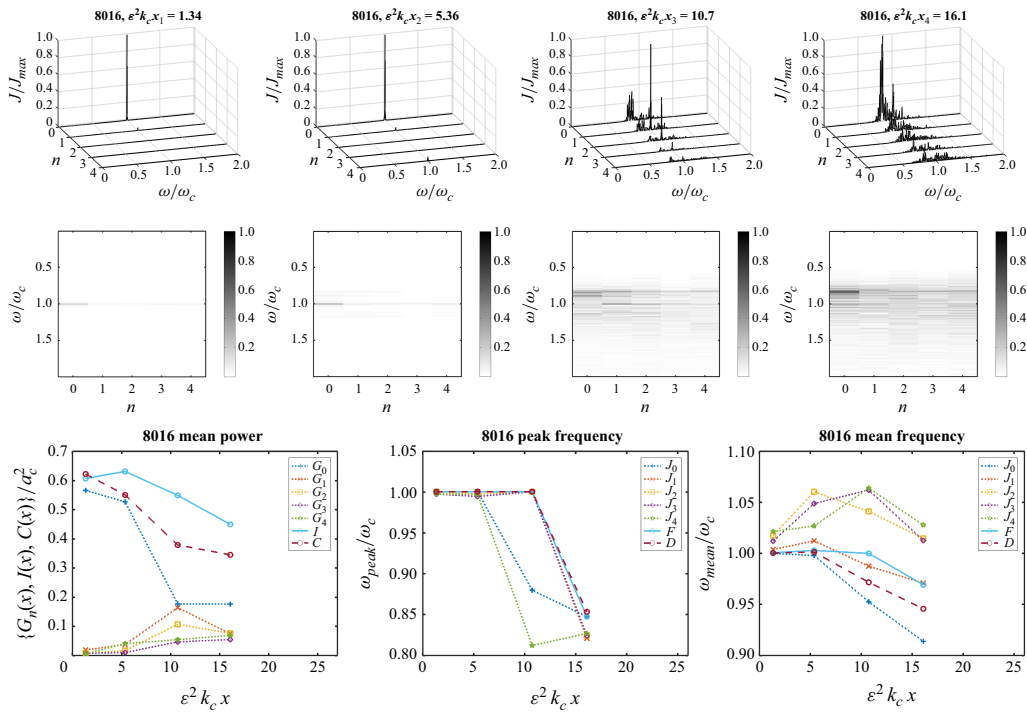


Figure 21. Run 8016.

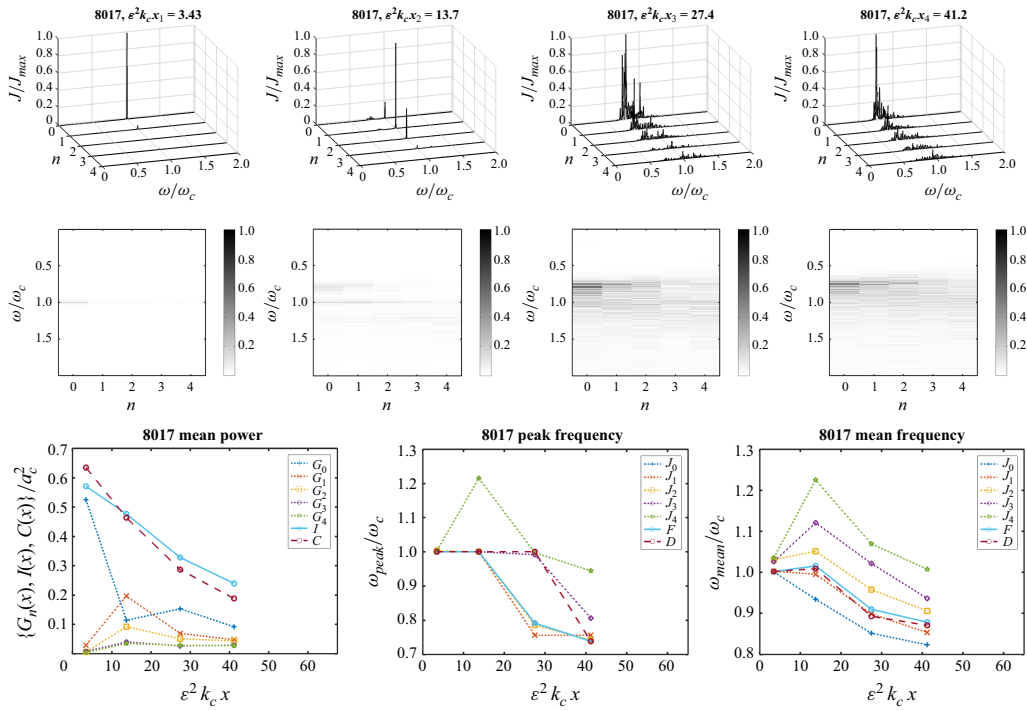


Figure 22. Run 8017.

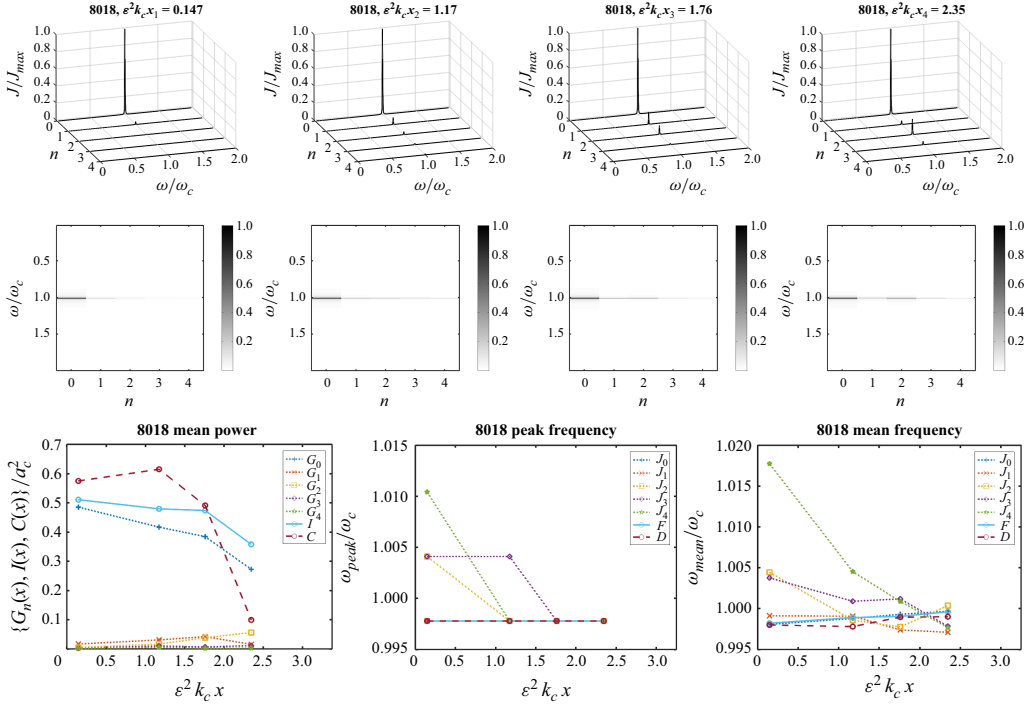


Figure 23. Run 8018.

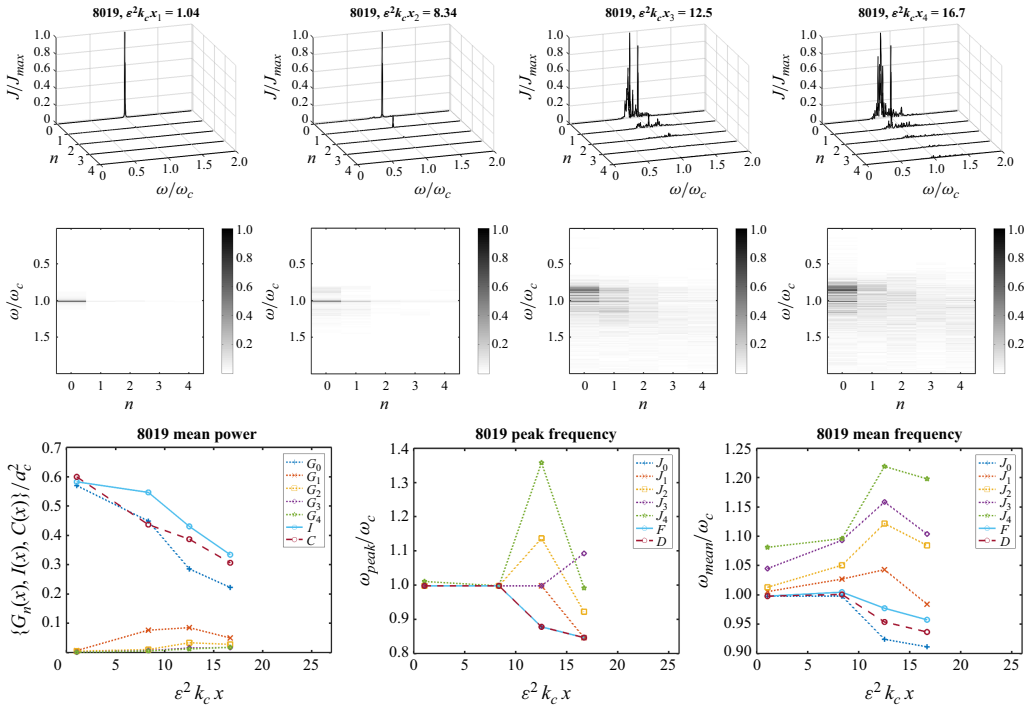


Figure 24. Run 8019.



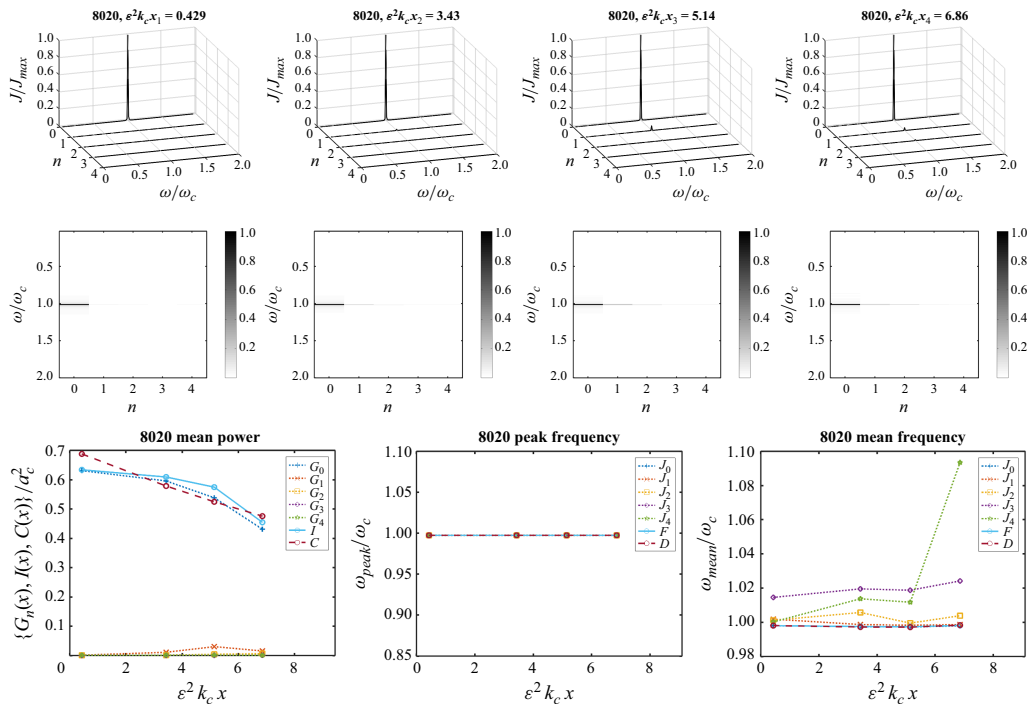


Figure 25. Run 8020.

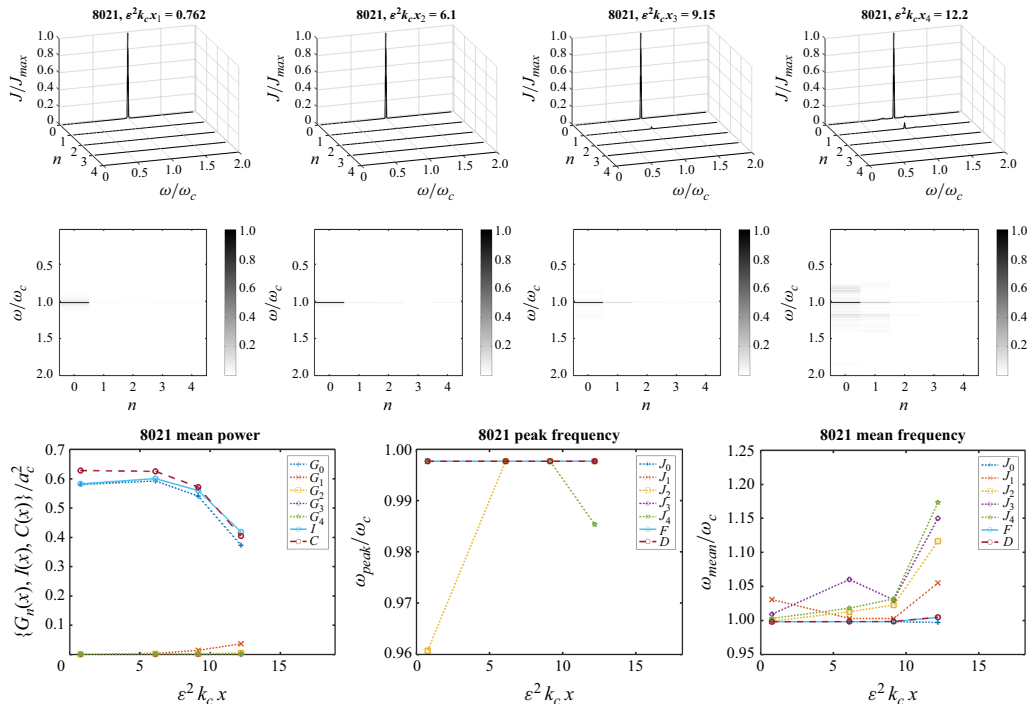


Figure 26. Run 8021.

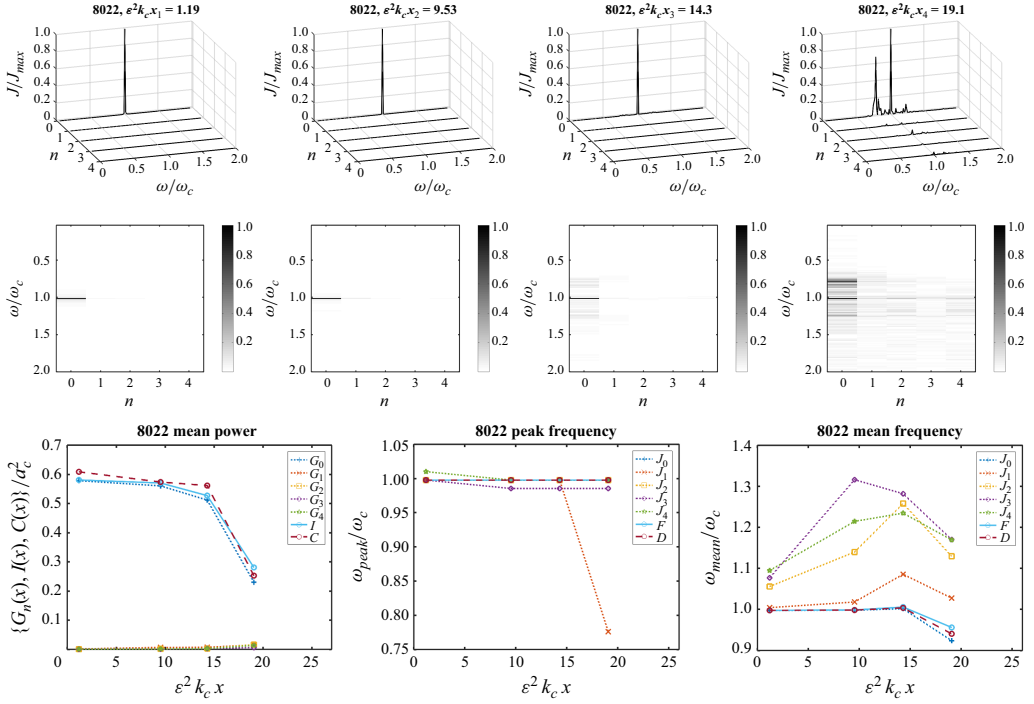


Figure 27. Run 8022.

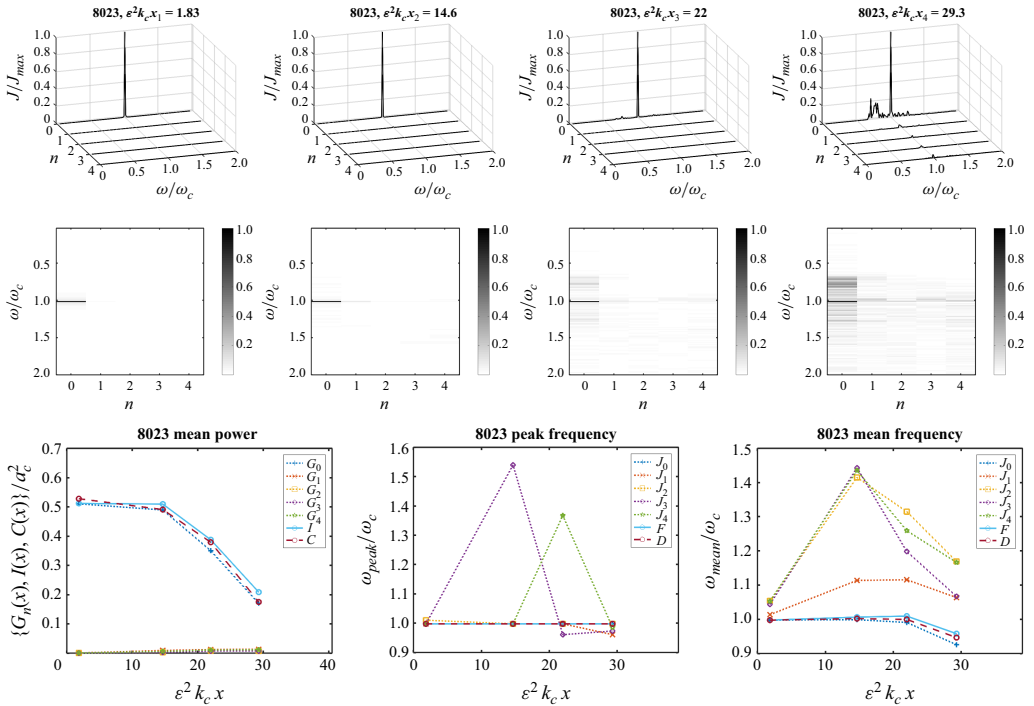


Figure 28. Run 8023.

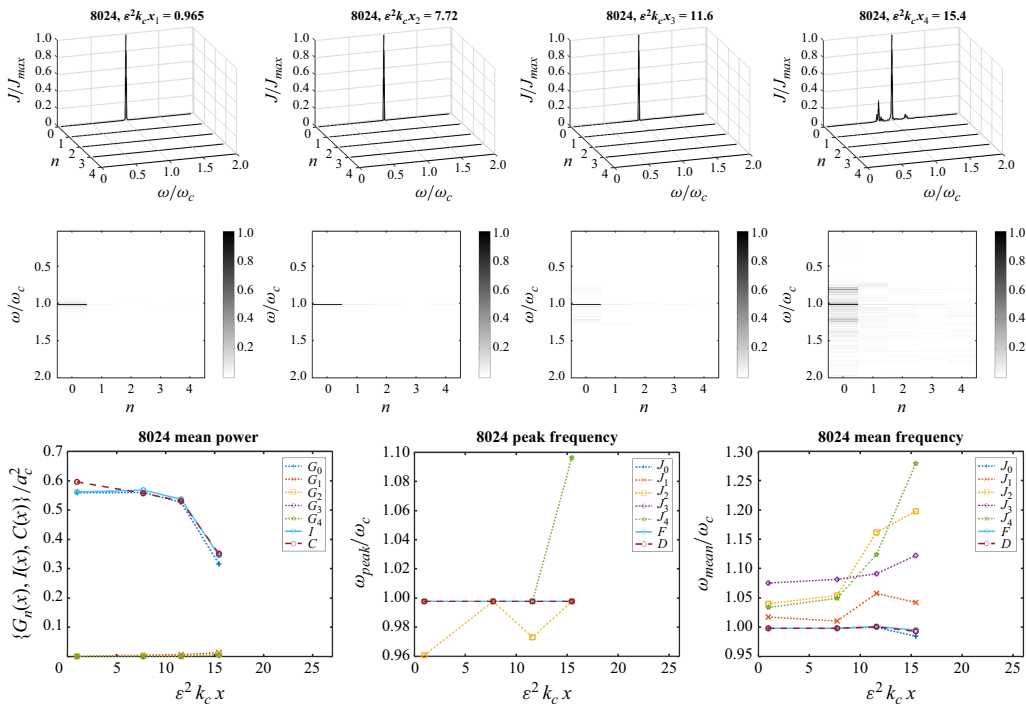


Figure 29. Run 8024.

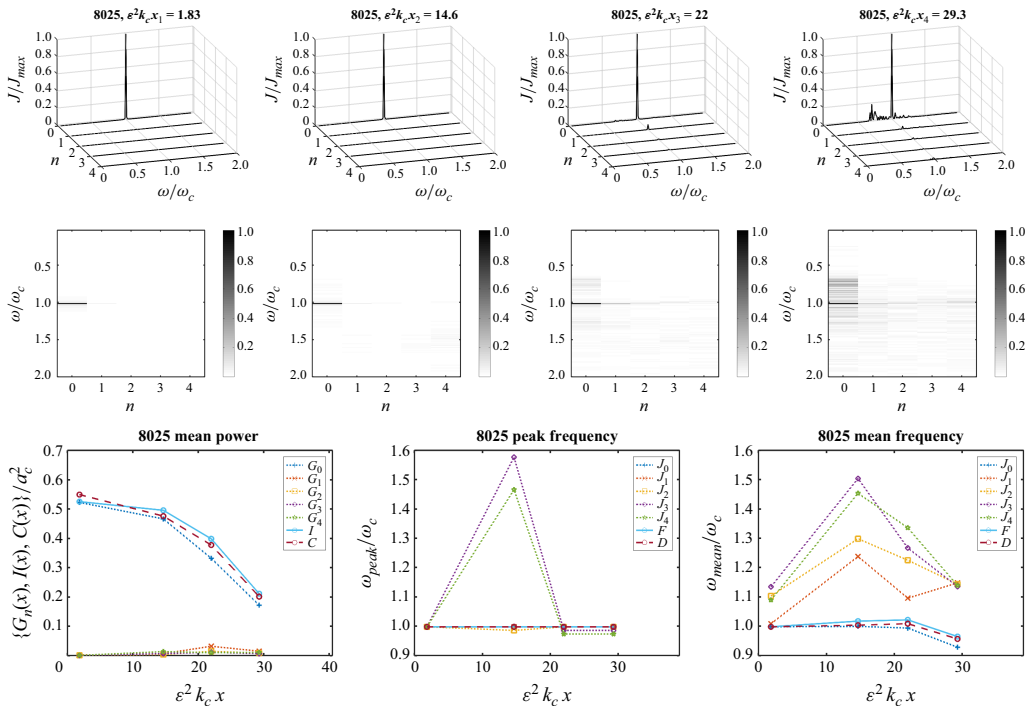


Figure 30. Run 8025.

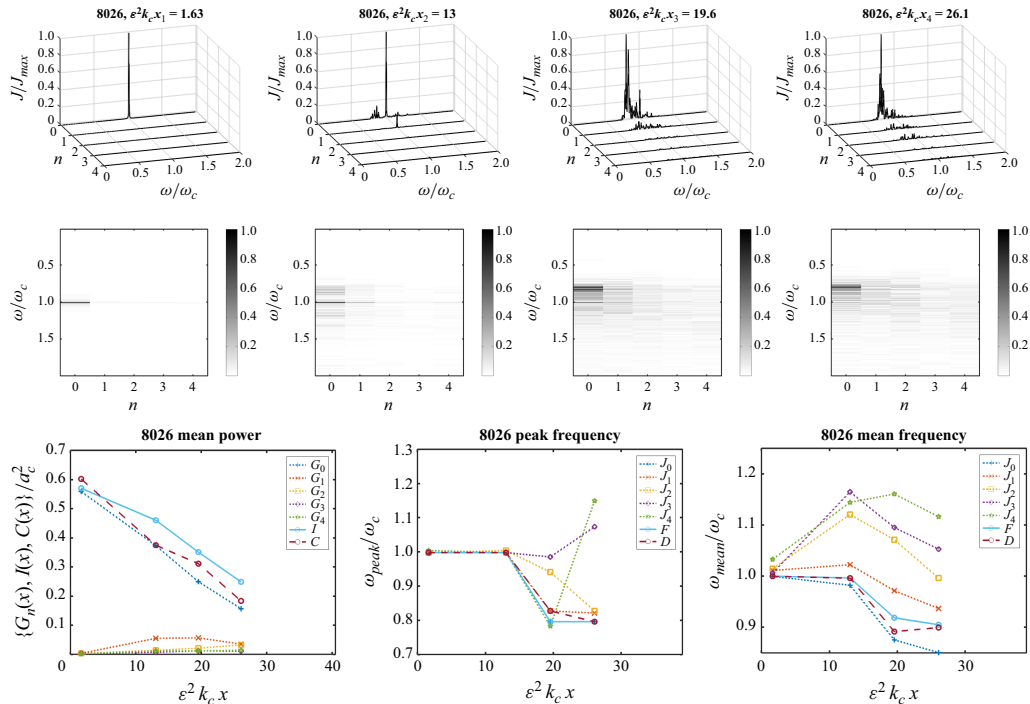


Figure 31. Run 8026.

**Appendix B. Pictures from various runs**

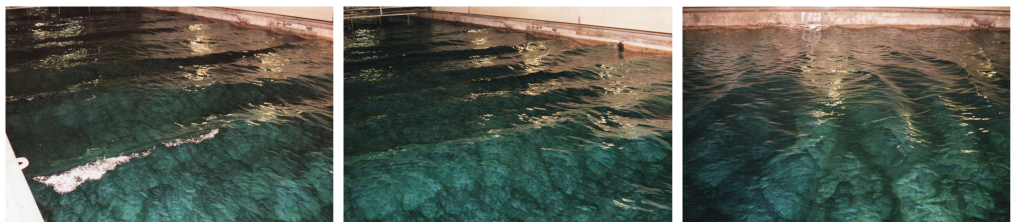


Figure 32. Pictures from run 8008.



Figure 33. Pictures from run 8009.



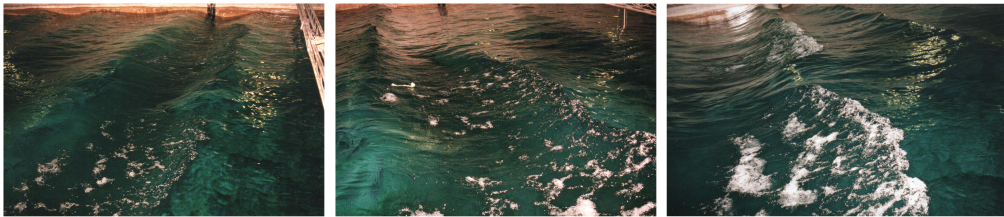


Figure 34. Pictures from run 8010.



Figure 35. Pictures from run 8011.

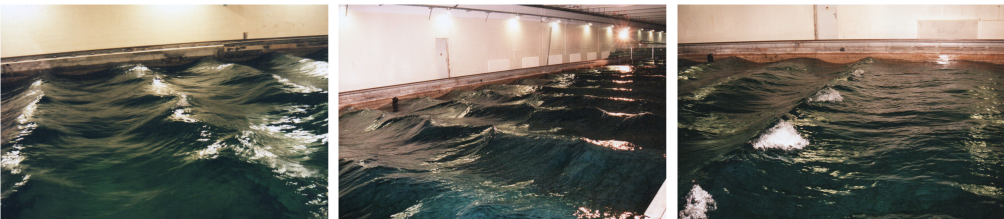


Figure 36. Pictures from run 8012.



Figure 37. Pictures from run 8013.



Figure 38. Pictures from run 8014.



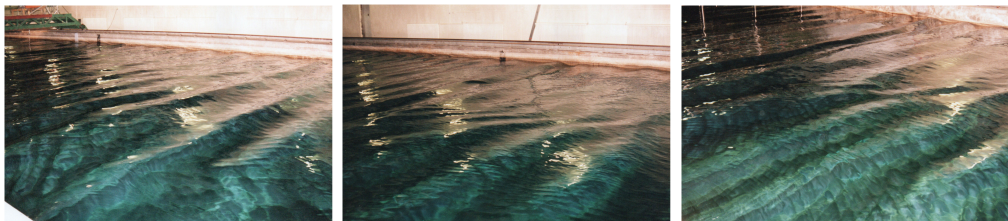


Figure 39. Pictures from run 8015.



Figure 40. Pictures from run 8016.

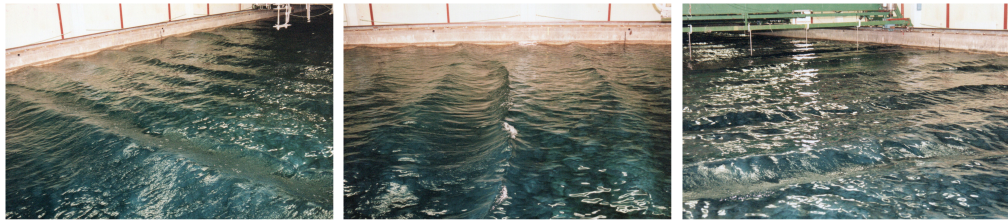


Figure 41. Pictures from run 8017.

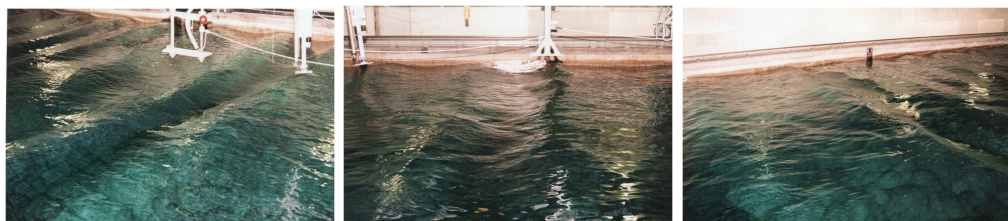


Figure 42. Pictures from run 8019.



Figure 43. Pictures from run 8025.

REFERENCES

- ALBER, I.E. 1978 The effects of randomness on the stability of two-dimensional surface wavetrains. *Proc. R. Soc. Lond. A* **363**, 525–546.
- BENJAMIN, T.B. 1967 Instability of periodic wavetrains in nonlinear dispersive systems. *Proc. R. Soc. Lond. A* **299**, 59–75.
- BENJAMIN, T.B. & FEIR, J.E. 1967 The disintegration of wave trains on deep water. *J. Fluid Mech.* **27**, 417–430.
- BENNEY, D.J. & ROSKES, G.J. 1969 Wave instabilities. *Stud. Appl. Maths* **48**, 377–385.
- CARTER, J.D., HENDERSON, D. & BUTTERFIELD, I. 2019 A comparison of frequency downshift models of wave trains on deep water. *Phys. Fluids* **31** (1), 013103.
- CHALIKOV, D. 2012 On the nonlinear energy transfer in the unidirectional adiabatic surface waves. *Phys. Lett. A* **376**, 2795–2798.
- CHERNEVA, Z. & GUEDES SOARES, C. 2011 Evolution of wave properties during propagation in a ship towing tank and an offshore basin. *Ocean Engng* **38**, 2254–2261.
- DAUXOIS, T. 2008 Fermi, Pasta, Ulam, and a mysterious lady. *Phys. Today* **61**, 55–57.
- DYSTHE, K.B. 1979 Note on a modification to the nonlinear Schrödinger equation for application to deep water waves. *Proc. R. Soc. Lond. A* **369**, 105–114.
- DYSTHE, K.B., TRULSEN, K., KROGSTAD, H.E. & SOCQUET-JUGLARD, H. 2003 Evolution of a narrow band spectrum of random surface gravity waves. *J. Fluid Mech.* **478**, 1–10.
- FERMI, E., PASTA, J. & ULAM, S. 1955 Report LA-1940. Tech. Rep. Los Alamos Scientific Laboratory.
- FERNANDEZ, L., ONORATO, M., MONBALIU, J. & TOFFOLI, A. 2014 Modulational instability and wave amplification in finite water depth. *Nat. Hazards Earth Syst. Sci.* **14**, 705–711.
- FUHRMAN, D.R., MADSEN, P.A. & BINGHAM, H.B. 2006 Numerical simulation of lowest-order short-crested wave instabilities. *J. Fluid Mech.* **563**, 415–441.
- GRAMSTAD, O. & TRULSEN, K. 2007 Influence of crest and group length on the occurrence of freak waves. *J. Fluid Mech.* **582**, 463–472.
- HARA, T. & MEI, C.C. 1991 Frequency downshift in narrowbanded surface waves under the influence of wind. *J. Fluid Mech.* **230**, 429–477.
- HASIMOTO, H. & ONO, H. 1972 Nonlinear modulation of gravity waves. *J. Phys. Soc. Japan* **33**, 805–811.
- ISLAS, A. & SCHOBER, C.M. 2011a Rogue waves and downshifting in the presence of damping. *Nat. Hazards Earth Syst. Sci.* **11**, 383–399.
- ISLAS, A. & SCHOBER, C.M. 2011b Rogue waves, dissipation, and downshifting. *Physica D* **240**, 1041–1054.
- JANSSEN, P.A.E.M. 1981 Modulational instability and the Fermi–Pasta–Ulam recurrence. *Phys. Fluids* **24**, 23–26.
- JANSSEN, P.A.E.M. 1983 On a fourth-order envelope equation for deep-water waves. *J. Fluid Mech.* **126**, 1–11.
- KATO, Y. & OIKAWA, M. 1995 Wave number downshift in modulated wavetrain through a nonlinear damping effect. *J. Phys. Soc. Japan* **64**, 4660–4669.
- LAKE, B.M., YUEN, H.C., RUNGALDIER, H. & FERGUSON, W.E. 1977 Nonlinear deep-water waves: theory and experiment. Part 2: evolution of a continuous wave train. *J. Fluid Mech.* **83**, 49–74.
- LIGHTHILL, M.J. 1965 Contributions to the theory of waves in non-linear dispersive systems. *IMA J. Appl. Maths* **1**, 269–306.
- LO, E. & MEI, C.C. 1985 A numerical study of water-wave modulation based on a higher-order nonlinear Schrödinger equation. *J. Fluid Mech.* **150**, 395–416.
- LO, E.Y. & MEI, C.C. 1987 Slow evolution of nonlinear deep water waves in two horizontal directions: a numerical study. *Wave Motion* **9**, 245–259.
- MCLEAN, J.W., MA, Y.C., MARTIN, D.U., SAFFMAN, P.G. & YUEN, H.C. 1981 Three-dimensional instability of finite-amplitude water waves. *Phys. Rev. Lett.* **46**, 817–820.
- MELVILLE, W.K. 1982 The instability and breaking of deep-water waves. *J. Fluid Mech.* **115**, 165–185.
- ONORATO, M. *et al.* 2009 Statistical properties of mechanically generated surface gravity waves: a laboratory experiment in a three dimensional wave basin. *J. Fluid Mech.* **627**, 235–257.
- ONORATO, M., OSBORNE, A.R., SERIO, M., RESIO, D., PUSHKAREV, A., ZAKHAROV, V.E. & BRANDINI, C. 2002 Freely decaying weak turbulence for sea surface gravity waves. *Phys. Rev. Lett.* **89**, 144501-1–144501-4.
- PINHO, U.F. & BABANIN, A.V. 2015 Emergence of short crestedness in originally unidirectional nonlinear waves. *Geophys. Res. Lett.* **42**, 4110–4115.
- RATLIFF, D.J., TRICHTCHENKO, O. & BRIDGES, T.J. 2025 Modulation leading to frequency downshifting of water waves in the vicinity of the Benjamin–Feir transition. *J. Fluid Mech.* **1014**, A23.

- SCHOBER, C.M. & STRAWN, M. 2015 The effects of wind and nonlinear damping on rogue waves and permanent downshift. *Physica D* **313**, 81–98.
- SEGUR, H., HENDERSON, D., CARTER, J., HAMMACK, J., LI, C.-M., PHEIFF, D. & SOCHA, K. 2005 Stabilizing the Benjamin–Feir instability. *J. Fluid Mech.* **539**, 229–271.
- SKANDRANI, C., KHARIF, C. & POITEVIN, J. 1996 Nonlinear evolution of water surface waves: the frequency down-shift phenomenon. *Contemp. Maths* **200**, 157–171.
- STOKES, G.G. 1847 On the theory of oscillatory waves. *Trans. Camb. Phil. Soc.* **8**, 441–455.
- SU, M.-Y. 1982 Three-dimensional deep-water waves. Part 1. Experimental measurement of skew and symmetric wave patterns. *J. Fluid Mech.* **124**, 73–108.
- SU, M.-Y., BERGIN, M., MARLER, P. & MYRICK, R. 1982 Experiments on nonlinear instabilities and evolution of steep gravity-wave trains. *J. Fluid Mech.* **124**, 45–72.
- TOFFOLI, A. *et al.* 2013 Experimental evidence of the modulation of a plane wave to oblique perturbations and generation of rogue waves in finite water depth. *Phys. Fluids* **25**, 091701.
- TOFFOLI, A., GRAMSTAD, O., TRULSEN, K., MONBALIU, J., BITNER-GREGERSEN, E. & ONORATO, M. 2010 Evolution of weakly nonlinear random directional waves: laboratory experiments and numerical simulations. *J. Fluid Mech.* **664**, 313–336.
- TRULSEN, K. & DYSTHE, K.B. 1990 Frequency down-shift through self modulation and breaking. *Water Wave Kinematics* (ed. A. Tørum & O.T. Gudmestad), pp. 561–572. Kluwer.
- TRULSEN, K. & DYSTHE, K.B. 1992 Action of windstress and breaking on the evolution of a wavetrain. In *Breaking Waves* (ed. M.L. Banner & R.H.J. Grimshaw), pp. 243–249. Springer.
- TRULSEN, K. & DYSTHE, K.B. 1997 Frequency downshift in three-dimensional wave trains in a deep basin. *J. Fluid Mech.* **352**, 359–373.
- TRULSEN, K., STANSBERG, C.T. & VELARDE, M.G. 1999 Laboratory evidence of three-dimensional frequency downshift of waves in a long tank. *Phys. Fluids* **11**, 235–237.
- TULIN, M.P. 1996 Breaking of ocean waves and downshifting. In *Waves and Nonlinear Processes in Hydrodynamics* (ed. Grue J., Gjevik B. & Weber J.E.), pp. 177–190. Kluwer.
- TULIN, M.P. & WASEDA, T. 1999 Laboratory observations of wave group evolution, including breaking effects. *J. Fluid Mech.* **378**, 197–232.
- UCHIYAMA, Y. & KAWAHARA, T. 1994 A possible mechanism for frequency down-shift in nonlinear wave modulation. *Wave Motion* **20**, 99–110.
- YUEN, H.C. & FERGUSON, W.E. 1978*a* Fermi–Pasta–Ulam recurrence in the two-space dimensional nonlinear Schrödinger equation. *Phys. Fluids* **21**, 2116–2118.
- YUEN, H.C. & FERGUSON, W.E. 1978*b* Relationship between Benjamin–Feir instability and recurrence in the nonlinear Schrödinger equation. *Phys. Fluids* **21**, 1275–1278.